

AD-A032 429

DAYTON UNIV OHIO RESEARCH INST
WATER DROP BREAKUP/IMPACT DAMAGE THRESHOLDS.(U)

F/G 16/3

JUL 76 J P BARBER
UDRI-TR-76-55

F33615-76-C-5038

UNCLASSIFIED

AFML-TR-76-126

NL

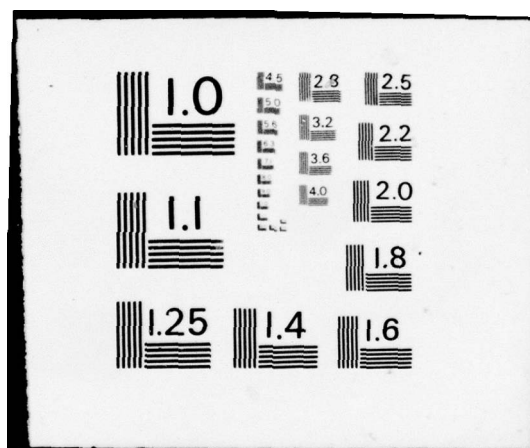
1 OF 1
ADA032429



END

DATE
FILMED

1 - 77



ADA032429

AFML-TR-76-126

12
NW

WATER DROP BREAKUP/IMPACT DAMAGE THRESHOLDS

UNIVERSITY OF DAYTON RESEARCH INSTITUTE
300 COLLEGE PARK
DAYTON, OHIO 45459

JULY 1976

FINAL REPORT FOR PERIOD JULY 1975 - JULY 1976

DDC
REF ID: A62112
NOV 23 1976
B

Approved for public release; distribution unlimited

AIR FORCE MATERIALS LABORATORY
AIR FORCE WRIGHT AERONAUTICAL LABORATORIES
AIR FORCE SYSTEMS COMMAND
WRIGHT-PATTERSON AIR FORCE BASE, OHIO 45433

NOTICE

When Government drawings, specifications, or other data are used for any purpose other than in connection with a definitely related Government procurement operation, the United States Government thereby incurs no responsibility nor any obligation whatsoever; and the fact that the government may have formulated, furnished, or in any way supplied the said drawings, specifications, or other data, is not to be regarded by implication or otherwise as in any manner licensing the holder or any other person or corporation, or conveying any rights or permission to manufacture, use, or sell any patented invention that may in any way be related thereto.

This technical report has been reviewed and is approved for publication.

Glenn Ormbrek
Glenn Ormbrek, AFML/MXS
Project Engineer

FOR THE DIRECTOR:

Henry E. Keck
Henry E. Keck, Major, USAF
Chief, Space and Missiles Branch
Systems Support Division
Air Force Materials Laboratory

ACCESSION FOR	
RTIS	White Section <input checked="" type="checkbox"/>
	Gold Section <input type="checkbox"/>
CD	<input type="checkbox"/>
DISTRIBUTION	
BY	
DISTRIBUTION/AVAILABILITY CODES	
DIR.	AVAIL. END OR SPECIAL
A	

Copies of this report should not be returned unless return is required by security considerations, contractual obligations, or notice on a specific document.

UNCLASSIFIED

SECURITY CLASSIFICATION OF THIS PAGE (When Data Entered)

19 REPORT DOCUMENTATION PAGE		READ INSTRUCTIONS BEFORE COMPLETING FORM
1. REPORT NUMBER AFML-TR-76-126	2. GOVT ACCESSION NO.	3. PECIPENT'S CATALOG NUMBER
4. TITLE (and Subtitle) WATER DROP BREAKUP/IMPACT DAMAGE THRESHOLDS.		5. TYPE OF REPORT & PERIOD COVERED Final Technical Report. Jul 1975 - Jul 1976
6. AUTHOR(s) Dr. John P. Barber		7. PERFORMING ORG. REPORT NUMBER UDRI-TR-76-55
8. CONTRACT OR GRANT NUMBER(s) F33615-76-C-5038 new		9. PERFORMING ORGANIZATION NAME AND ADDRESS University of Dayton 300 College Park Dayton OH 45469
10. PROGRAM ELEMENT, PROJECT, TASK AREA & WORK UNIT NUMBERS 1264p. 63311F 627AD034		11. CONTROLLING OFFICE NAME AND ADDRESS Air Force Materials Laboratory (MXS) Wright-Patterson AFB, Ohio 45433
12. REPORT DATE Jul 1976		13. NUMBER OF PAGES 56
14. MONITORING AGENCY NAME & ADDRESS (if different from Controlling Office)		15. SECURITY CLASS. (of this report) UNCLASSIFIED
16. DISTRIBUTION STATEMENT (of this Report) Approved for public release; distribution unlimited.		15a. DECLASSIFICATION/DOWNGRADING SCHEDULE
17. DISTRIBUTION STATEMENT (of the abstract entered in Block 20, if different from Report)		
18. SUPPLEMENTARY NOTES		
19. KEY WORDS (Continue on reverse side if necessary and identify by block number) Erosion, Hypervelocity Erosion, Rain Erosion, Impact, Water Droplets, Droplet Impact, Reentry Vehicle, Bow Shocks 20-1 to 100-micrometer		
20. ABSTRACT (Continue on reverse side if necessary and identify by block number) An investigation of the breakup criteria for water droplets traversing reentry vehicle bow shocks was conducted. Hemispherical, ATJS graphite tipped, 20 mm projectiles were launched at reentry velocities (2.5 km/s to 4.5 km/s) into a single stream of well separated, cloud sized water droplets (20 ^{mm} to 100 ^{mm} diameter). The projectile nosetip was observed about 1 ^{μm} after impact with the droplets. If the droplets survived transit through the shock layer, impact debris plumes were observed. If the droplets broke up in the shock layer, impact debris was not observed. The bow shock layer aerodynamic conditions were		

UNCLASSIFIED

SECURITY CLASSIFICATION OF THIS PAGE(When Data Entered)

20. ABSTRACT (continued)

→ systematically varied to investigate the transition (breakup criteria) over a range of Weber numbers (We) from about 20,000 to 160,000. The results showed good agreement with previous indirect measurements of breakup.

UNCLASSIFIED

SECURITY CLASSIFICATION OF THIS PAGE(When Data Entered)

PREFACE

The development described in this report was carried out by the University of Dayton at the Air Force Materials Laboratory, Wright-Patterson Air Force Base, Dayton, Ohio, under contract F33615-76-C-5038.

The work was conducted during the period July 1975, to July 1976, and was monitored by Mr. Glenn Ormbrek of the Air Force Materials Laboratory.

The author would like to thank those who contributed so much to this investigation. From UDRI, Mike Nagy who patiently endured the vagaries of the hypervelocity range and a perverse experiment, and Judy Steppel who laboriously read and reduced all the data several times, are especially acknowledged. The interest and assistance of Dr. Alan Hopkins and Mr. Glenn Ormbrek of the Air Force Materials Laboratory was greatly appreciated.

This report was submitted by the authors in May 1976, for publication as an AFML Technical Report.

TABLE OF CONTENTS

SECTION	PAGE
I INTRODUCTION	1
II DROPLET BREAKUP	2
2.1 Droplet Dilatation	3
2.2 Droplet Stripping/Breakup	4
2.3 Droplet Impact	5
III THE EXPERIMENT	7
3.1 The Range	7
3.2 The Investigation	8
IV RESULTS AND DISCUSSION	11
4.1 Droplet Breakup Observations	11
4.2 Droplet Impact Observations	11
4.3 Experimental Uncertainties and Errors	26
V CONCLUSIONS	39
REFERENCES	41
APPENDIX A	42
APPENDIX B	50

LIST OF FIGURES

FIGURE		PAGE
1	Droplet dilatation versus nondimensional time at high Weber numbers. (Taken from Reinecke, et al. ¹ , Figure 23).	4
2	A schematic of the water droplet experimental setup.	7
3	A comparison of an unseparated stream of water droplets (a) and an electrostatically separated stream (b). The average droplet diameter in each case is $\approx 100 \mu\text{m}$.	9
4	A typical shadowgraph showing droplet breakup.	12
5	Droplet dilatation versus nondimensional time for 100 μm diameter drops.	14
6	A schematic of the post-impact conditions as observed shadowgraphically.	15
7	A typical droplet impact shadowgraph showing graphite impact debris.	16
8	A shadowgraph of an impact on tungsten carbide.	18
9	The nondimensional time at impact versus Weber number for 95-100 μm diameter droplets. The solid symbols indicate impacts in which debris was generated and the open symbols indicate impacts in which no debris was observed.	20
10	A shadowgraph showing impact debris produced by the impact of 35-40 μm diameter droplets on ATJS graphite.	22
11	A shadowgraph showing no impact debris on ATJS graphite after encounter with 35-40 μm diameter droplets.	23
12	The nondimensional time at impact versus Weber number for 35-40 μm diameter droplets. The open symbols represent impacts in which no debris was observed. The closed symbols represent impacts in which debris was observed and the half-closed symbols represent impacts in which debris was only marginally detectable.	25
13	A shadowgraph of the encounter of an ATJS projectile with 25-30 μm droplets.	27
14	Nondimensional time-at-impact versus Weber number for 25-30 μm diameter droplets.	29
15	The geometry of off-center impacts.	35

LIST OF FIGURES (CONT'D)

FIGURE		PAGE
16	Shielded distance and debris plume height versus off-center displacement.	35
17	Nondimensional time at impact versus Weber number for all the data collected.	40

LIST OF TABLES

TABLE	PAGE
1 Water Droplet Breakup and Dilatation Data	13
2 90-100 μm Diameter Water Droplet Impacts	19
3 35-40 μm Diameter Water Droplet Impacts	24
4 25-30 μm Diameter Water Droplet Impacts	28
5 Estimated Data Errors	34
6 Estimated Errors in Reduced Data	34
7 Debris Plume Heights	36

SECTION I INTRODUCTION

Extensive investigations of water droplet breakup due to the passage of normal shocks have been conducted.^{(1), (2)} This work was carried out in shock tubes by dropping a stream of droplets across the tube and driving a shock wave over them. The behavior of the droplets in the shock flow region after passage of the shock was then investigated with photographic and x-radiographic techniques.

Two important modes of droplet breakup in typical hypervelocity reentry vehicle flow were identified: mass stripping and catastrophic breakup. In the mass-stripping mode, droplet mass is stripped away by the aerodynamic forces and the droplet eventually declines to "zero" mass. In the catastrophic mode of breakup, a Rayleigh-Taylor type of instability develops on the leading face of the droplet. The instability grows rapidly and the droplet disintegrates.

The implication of droplet breakup is that after the droplet has stripped to zero mass or disintegrated, it no longer presents an impact threat to the nosetip of a reentry vehicle. It is, therefore, important to identify what size of droplets will survive transit through a reentry vehicle shock layer, impact the vehicle surface, and inflict significant damage.

The work described in this report covers an investigation of the droplet breakup criteria conducted at the Air Force Materials Laboratory/University of Dayton Research Institute (AFML/UDRI) facility. A direct observation of droplet breakup and impact is used to determine the droplet impact threat. The results are compared with shock tube observations.

¹Reinecke, W. G., Waldman, G. D., McKay, W. L. and Ziering, M. B., "Shock Layer Shattering of Water Drops and Ice Crystals in Reentry Flight," AFML-TR-75-71.

²Jaffe, N. A., "Hydrometer Shock Interactions," Interim Technical Report, Contract DNA001-74-C-0051.

SECTION II DROPLET BREAKUP

The most direct observations of droplet breakup were made by Reinecke, Waldman, McKay and Ziering,⁽¹⁾ and their analysis and results will be reviewed briefly.

Reinecke, et al. observed the mass stripping and catastrophic breakup of rather large water droplets (500-2000 μm diameter) in a shock tube. Optical observations cannot differentiate density very well. Therefore, in order to observe the distribution of mass in a deforming drop and the residual mass in a stripping drop, Reinecke, et al. employed x-ray techniques. As the spatial resolution of x-radiography is not high (of the order of the source dimensions times the magnification minus one) they were limited to observing relatively large droplets (500 μm diameter and larger). Many observations of droplet stripping and breakup were obtained and the results are summarized in the following paragraphs.

Droplet behavior is conveniently described with a set of nondimensional variables including:

1. The Weber number, We , which is the ratio of the aerodynamic pressure to the surface tension of the drop. It is indicative of the mode in which the droplet will respond to the air flow. The Weber number is given by:

$$We = \frac{\rho v^2 D_o}{\sigma_l} \quad (1)$$

where ρ is the density of the air, v is the velocity air flow relative to the droplet, D_o is the diameter of the droplet and σ_l is the surface tension of the drop.

2. The nondimensional time, T , which is the time which the drop has resided in the shock region normalized to account for drop size and the density of the air and drop. It is given by:

$$T = \frac{vt}{D_o} \left(\frac{\rho}{\rho_d} \right)^{1/2} \quad (2)$$

where v is the velocity, t is the time after entrance into the shock, D_o is the droplet diameter, ρ is the air density of the shocked gas and ρ_d is the droplet density.

3. The nondimensional distance, X , which is simply distance normalized to the droplet diameter as:

$$X = x/D_o, \quad (3)$$

where x is the distance and D_o is the droplet diameter.

Typical values of these parameters in reentry erosion cloud environments are:

$$2 \text{ kg/m}^3 < \rho < 10 \text{ kg/m}^3 \quad (4)$$

$$2 \text{ km/s} < v < 6 \text{ km/s} \quad (5)$$

$$10 \mu\text{m} < D_o < 200 \mu\text{m} \quad (6)$$

$$\sigma_l = 0.072 \text{ N/m} \text{ (for pure water)} \quad (7)$$

$$1000 < We < 10^6 \quad (8)$$

In this report we shall concern ourselves with two aspects of the water droplet-bow shock interaction: drop dilatation and the stripping/breakup criterion.

2.1 DROPLET DILATATION

When a droplet enters the bow shock region of a reentry vehicle nosetip, high aerodynamic pressures are generated on the front or leading surface of the drop. The pressure declines toward the equator. The pressure gradient across the droplet causes it to flatten and the major diameter grows. A number of calculations of this dilatation have been carried out. At the high Weber number ($>>1000$) of interest here, droplet dilatation is found to vary at early times as T^2 and at later times as T . Reinecke, et al.⁽¹⁾ compared their experimental results to the theoretical predictions and found reasonable agreement as shown in Figure 1. We shall present our results in Section 4.

Droplet dilatation was investigated in this study only to indicate whether or not the observed droplets breakup as expected. If the droplets observed display proper dilatation before impact we can be reasonably as-

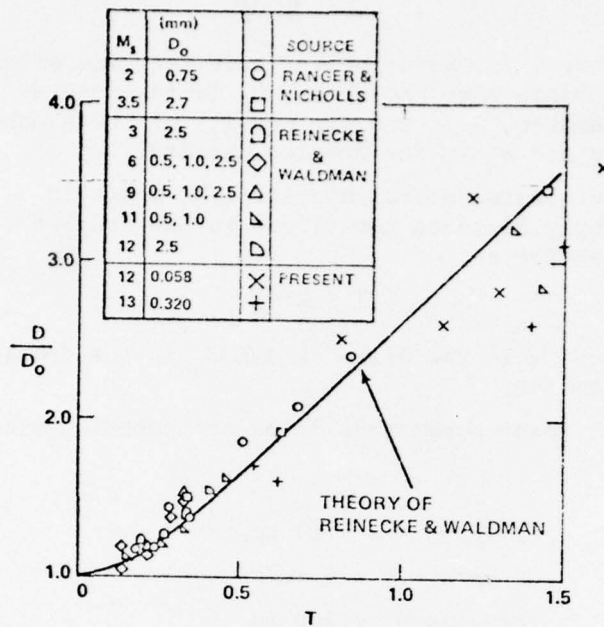


Figure 1. Droplet dilatation versus nondimensional time at high Weber numbers. (Taken from Reinecke, et al.¹, Figure 23).

sured that at impact, where they cannot be observed, they will have reached a predictable degree of dilatation, stripping and/or breakup.

2.2 DROPLET STRIPPING/BREAKUP

Reinecke, et al.¹ found that the mode of droplet breakup depends on the Weber number. For the Weber numbers of interest in reentry, the important modes are: mass stripping for Weber numbers greater than 100, and catastrophic breakup for Weber numbers greater than 20,000.

In the stripping mode, the drop flattens due to the aerodynamic forces and small droplets of water or mist are torn off the equator by the high aerodynamic forces in that region. Reinecke, et al. measured the droplet mass as a function of time in the stripping mode by the use of x-rays. Large water drops (≈ 1 mm) were dropped into a shock tube and a shock launched over them. X-radiographs of the droplets at various times after passage of the shock front were obtained; by measuring the optical density of the x-radiographs and integrating over the entire image, the total mass distribution of the drop were measured. They found that drop mass declined

as

$$\frac{m}{m_0} = \frac{1}{2} (1 + \cos \frac{\pi T}{T_s}) \quad (9)$$

where m_0 is the initial drop mass and T_s is the nondimensional time at which the mass reaches zero. From a number of observations it was found that

$$T_s = 3.5. \quad (10)$$

Other workers have measured T_s somewhat less directly (Ranger and Nichols³) and found $T_s = 5$. We shall consider $T_s = 3.5$.

At high Weber numbers ($\sim 20,000$) the droplets lose very little mass, then suddenly disintegrate. The nondimensional time at disintegration, T_b , is related to the Weber number by correlation as,

$$T_b Q_m^{1/2} = 35 We^{-1/4}, \quad (11)$$

for $We > 2700$ (Reinecke, et al.¹) where Q_m is the ratio of the dynamic pressure at the drop surface to the dynamic pressure of the air flow ahead of the drop. The range of nondimensional times of interest in hypervelocity erosion is described by stripping in which $T_s \approx 3.5$ when the droplet mass reaches zero, and catastrophic breakup in which $T_b Q_m^{1/2} \approx 35 We^{-1/4}$ when the droplet disintegrates.

2.3 DROPLET IMPACT

The implication of the droplet breakup correlations is that when a droplet has stripped to zero mass, or disintegrated, it no longer presents an erosive threat. That is, a droplet that has broken up will not impact the surface or cause significant damage. The remains of the droplet remain in the airflow and it is thought that the material is accelerated to the air velocity and swept around the vehicle.

These breakup criteria were established largely with x-radiographic measurements. Breakup was defined as the time at which an x-ray image of the distended or disintegrated droplet can no longer be obtained. This implies that the average density of the droplet has fallen below some critical level and insufficient x-rays are absorbed to generate

³Ranger, A. A. and Nichols J. A., "Aerodynamic Shattering of Liquid Droplets," AIAA Journal, 7:285-290, 1969.

a measurable image on the film. However, shadowphotography reveals that the droplet material is still present (the mass cannot, after all, simply disappear) confined to an area dimension not generally greater than about 10 times the original drop diameter. Moreover, previous observations⁽⁴⁾ made at the AFML/UDRI facility did not reveal any significant sweeping of drop debris around the nosetip. The distended drop is accelerated but appears to impact the nosetip at a significant fraction of the initial encounter velocity.

It is, therefore, important to conduct a more realistic appraisal of the breakup criteria. The critical x-radiographically detectable density of water does not seem, *per se*, to be a good damage threat criterion. Reinecke, et al.⁽¹⁾ conducted some direct tests of the breakup criteria with a cupped projectile in which the depth of the cup was varied to vary the shock standoff distance and the subsequent time to impact. The experiment was statistical in that only the average drop size and average impact frequency were known. However, good statistically significant data were obtained and were in agreement with the x-ray correlations, although a slightly longer time to apparent breakup was observed. The tests were conducted on drops with Weber numbers of about 600,000 so only the catastrophic mode of breakup was investigated.

We have undertaken a study of the breakup criteria which will extend over a wide range of Weber numbers typical of reentry conditions. The results reported herein cover a range of Weber numbers from about 20,000 to 160,000.

⁴Barber, J. P., Grood, E. S., Taylor, H. R. and Hopkins, A. K., "Water Drop/Bow Shock Interactions", AFML-TR-75-105.

SECTION III
THE EXPERIMENT

3.1 THE RANGE

The experiments were conducted on the AFML light gas gun range described by Barber et al.⁽⁴⁾ Briefly, a graphite-tipped 20 mm projectile is launched down a range into a free-falling stream of water drops. The encounter is observed with a high resolution, high magnification laser/microscope camera shown in Figure 2. Since the cited report⁽⁴⁾ was generated,

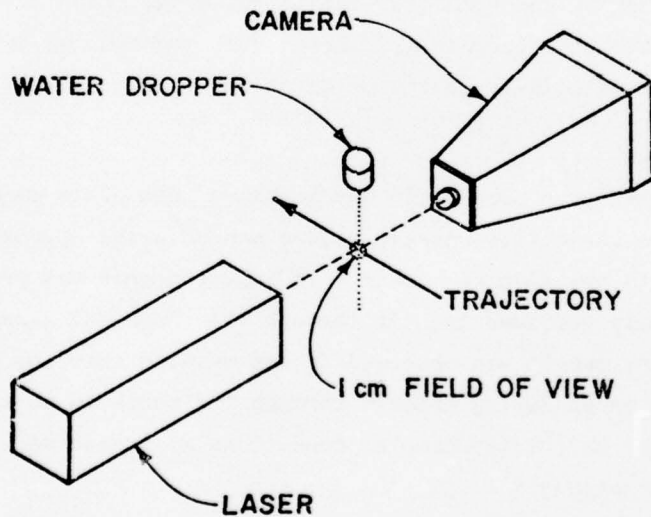


Figure 2. A schematic of the water droplet experimental setup.

a number of improvements have been carried out on the range:

1. A second camera was added to obtain a spark shadowgraph of the droplet field about 10 μ s before encounter with the oncoming projectile.

This permits accurate measurement of the size and position of the droplets before encounter and greatly aids in the interpretation of post-encounter information.

2. A droplet separator was devised which electrostatically extracts all but a selected number of drops in the free falling stream. The drops, when generated are separated by only about three diameters. The close proximity of the drops to one another resulted in unacceptable interference between the drops and the associated aerodynamic and impact effects. With the separation currently obtained no such coupling occurs. A comparison of the as-generated droplet stream and a separated stream is shown in Figure 3.

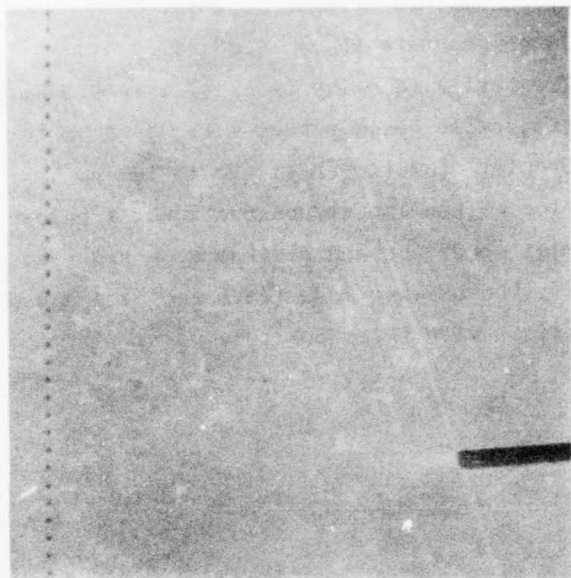
3. A guide rail system was installed on the range to guide the projectile from the gun muzzle to the test section. The system was patterned on the device developed by Teng et al.⁽⁵⁾ The projectiles are aerodynamically unstable and tend to yaw and fly off trajectory in free flight. As the field of view and depth of field of the camera are not large, this led to an unacceptably low return of good-quality unambiguous data. The installation of the guide rail system has largely eliminated this problem and has greatly improved the quality and utility of the observations.

3.2 THE INVESTIGATION

An ATJS graphite-tipped projectile was launched into a stream of well separated drops. The projectile nosetip region was observed approximately 1 μ s after impact with the droplet stream. If impact debris was present, the drops had obviously survived transit through the shock and damaged the surface. If no impact debris was observed it was assumed that the droplet was sufficiently broken up during transit through the shock to no longer present a threat. The calculated droplet conditions at impact were then compared to the correlations.

The range pressure, projectile velocity, projectile nosetip radius and droplet diameter were varied to systematically investigate the nondimensional time at impact as a function of the droplet Weber number.

⁵ Teng, R. N., Hickman, R. S. and Sutila, G. E., "Development of a Scaled-up Hypervelocity Projectile Guiding and Retrieving System", AEDC-TR-74-123, January 1975.



(a)



(b)

Figure 3. A comparison of an unseparated stream of water droplets (a) and an electrostatically separated stream (b). The average droplet diameter in each case is $\approx 100 \mu\text{m}$.

The following parameters were employed:

1. Range pressure (P_1): 0.33, 0.50 atm
2. Projectile velocity (v): ≈ 2.5 to 4.5 km/s
3. Projectile nosetip radius (R_N): 9 mm to ∞ (flat)
4. Droplet diameter (D_o): 20 to $100 \mu\text{m}$

In addition to the impact observations, a number of observations were made of droplet condition and breakup mode prior to impact. These observations verify the breakup mode (catastrophic) and provide additional direct comparison with the shock tube work.

SECTION IV
RESULTS AND DISCUSSION

4.1 DROPLET BREAKUP OBSERVATIONS

Observations of well-separated $\approx 100 \mu\text{m}$ diameter droplets at various stages of breakup were made. A typical shadowgraph is shown in Figure 4 and the data from all the shots are summarized in Table 1. As expected at these high Weber numbers, the mode of breakup is catastrophic disintegration and the presence of unstable surface waves on the leading faces of the droplets is clearly evident, especially at late times. Very little mass stripping is observed; the droplet wakes are relatively free of water vapor.

The dilatation of each observable droplet was measured and the results are shown in Figure 5 together with the theoretical predictions of Reinecke, et al.⁽¹⁾ The dilatation agrees very well with predictions at early times but there is appreciable scatter at later times. Reinecke, et al. also observed this scatter as shown in Figure 1 and their results including scatter are almost indistinguishable from those obtained here.

The scatter at late times is most probably due to the statistical growth of the disintegrating instability. In addition, the instability is probably not cylindrically symmetrical and the observed dilatation will depend on the random orientation of the drop.

4.2 DROPLET IMPACT OBSERVATIONS

Observations of the projectile nosetip were made approximately 1 μs after impact. The impact situation as observed is illustrated in Figure 6. The time after impact was chosen to permit any impact debris generated by the impact to exit from the surface sufficient distance to be detected on the laser/microscope camera shadowgraphs. A typical shadowgraph of impact-generated debris is shown in Figure 7.

The debris evident in Figure 7 may not all be graphite; some could presumably be droplet water ejected during the impact. As the occurrence of damage is based on observations of debris, it is important to establish if a significant part of the observed debris is water. Accordingly, conditions almost identical to these occurring in Figure 7 were repeated with the ATJS graphite nosetip replaced with a tungsten carbide nosetip. Tungsten

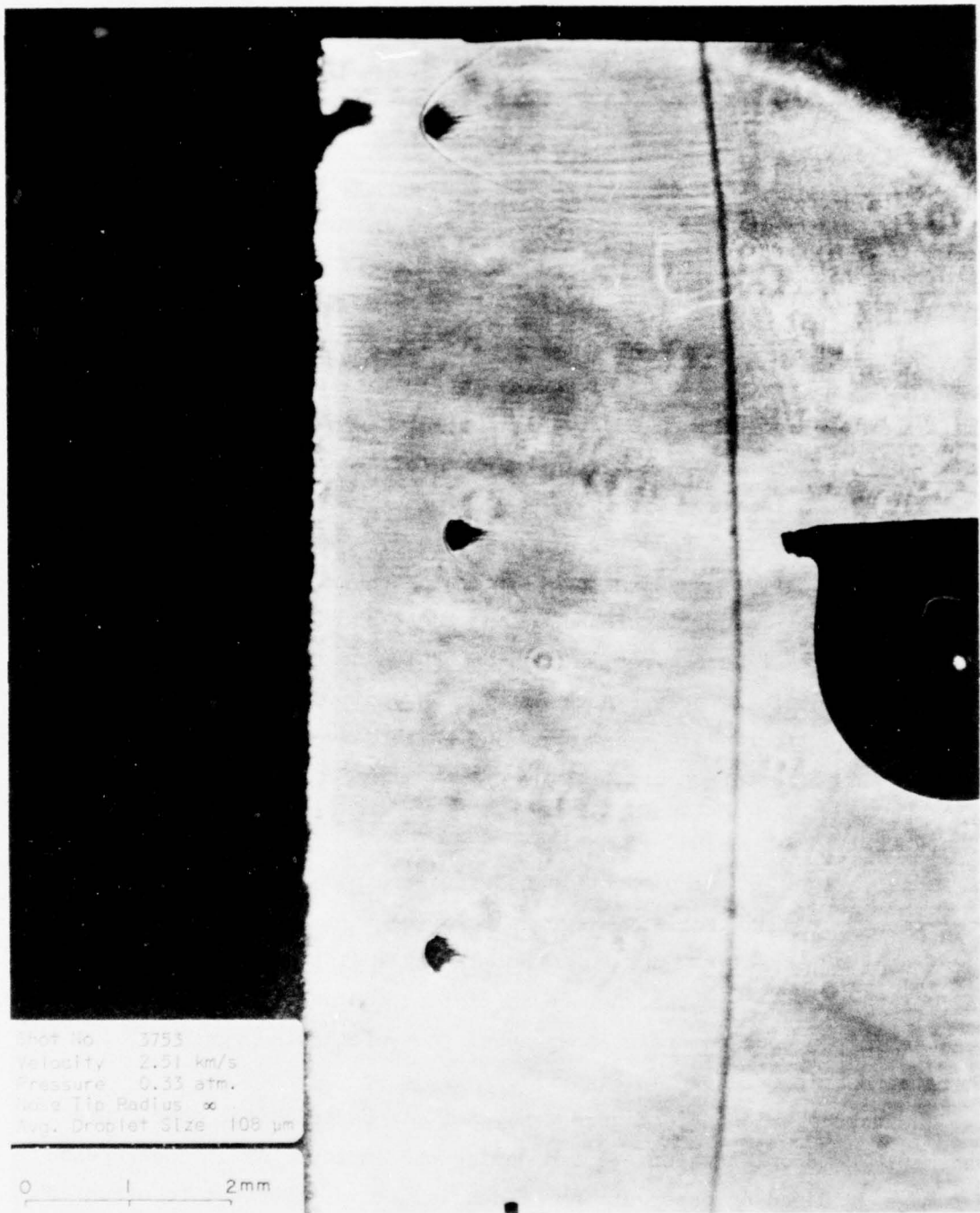


Figure 4. A typical shadowgraph showing droplet breakup.

TABLE 1. WATER DROPLET BREAKUP AND DILATATION DATA

Shot No.	R_N (mm)	P_1 (atm)	V (km/s)	ρ_{air} No.	ρ_2/ρ_1	ρ_2 (kg/m ³)	$\sqrt{\rho_2/\rho_1}$	Drop No.	D_0 (μm)	D (μm)	D/D_0	Number No.	x (mm)	T
3753	∞	0.33	2.79	3.1	7.5	2.97	5.45×10^{-2}	1	114	570	2.81	36.6	2.92	1.41
								2	104	521	3.09	33.4	2.97	1.57
								3	107	380	5.63	34.4	3.07	1.62
3754	∞	0.67	2.72	7.9	7.2	5.79	7.61×10^{-2}	1	80*	221	2.76	47.6	1.67	1.53
								2	86	251	3.05	69.1	2.05	1.79
								3	80	250	3.13	47.6	2.24	2.13
								4	77	270	3.51	45.8	1.82	1.83
								5	81	271	3.35	43.2	1.82	1.95
								6	76	268	3.53	45.2	1.82	1.62
								Avg.	80					
3756	∞	0.67	2.61	7.6	7.1	5.71	7.56×10^{-2}	1	107	305	2.85	57.8	1.55	0.96
								2	106	246	2.70	57.3	1.67	1.70
								3	109	261	2.39	58.9	1.61	1.12
								4	109	245	2.29	57.8	1.41	1.00
3757	∞	0.67	2.84	8.2	7.4	5.92	7.59×10^{-2}	1	110	318	2.89	72.9	2.54	1.64
								2	92	354	3.85	51.0	2.60	2.18
								3	95	318	3.35	53.0	2.66	2.15
								4	100	323	3.28	56.3	2.35	1.96
								Avg.	99					
3759	∞	0.67	2.85	8.3	7.5	6.00	7.75×10^{-2}	1	100	331	3.31	67.7	2.55	1.93
								2	93	286	3.08	65.0	2.76	2.31
								3	107	362	3.38	72.4	2.92	2.13
								4	95	375	3.95	64.5	2.71	2.23
3763	∞	0.50	3.01	8.7	7.8	4.68	6.84×10^{-2}	1	105	249	2.37	61.8	1.57	0.89
								2	108	292	2.72	63.6	1.50	0.94
								Avg.	107					

R_N nose tip radius
 P_1 range pressure
 V projectile velocity

ρ_{air} air density in range
 ρ_2 air density behind shock

P_d droplet density
 D_0 droplet initial diameter
 D droplet dilatation
 x distance from shock front to droplet
 t nondimensional shock residence time

* droplet diameter not measurable, average used

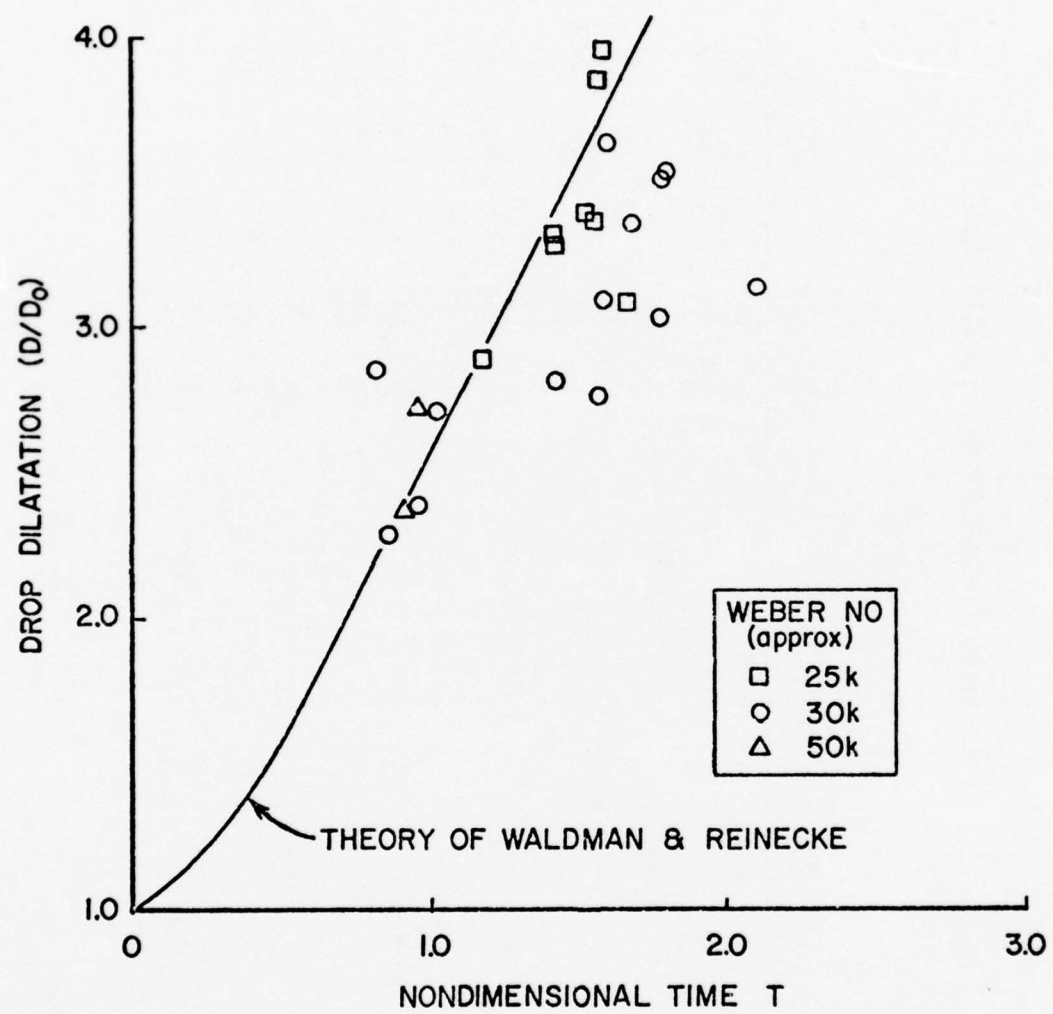


Figure 5. Droplet dilatation versus nondimensional time for 100 μm diameter drops.

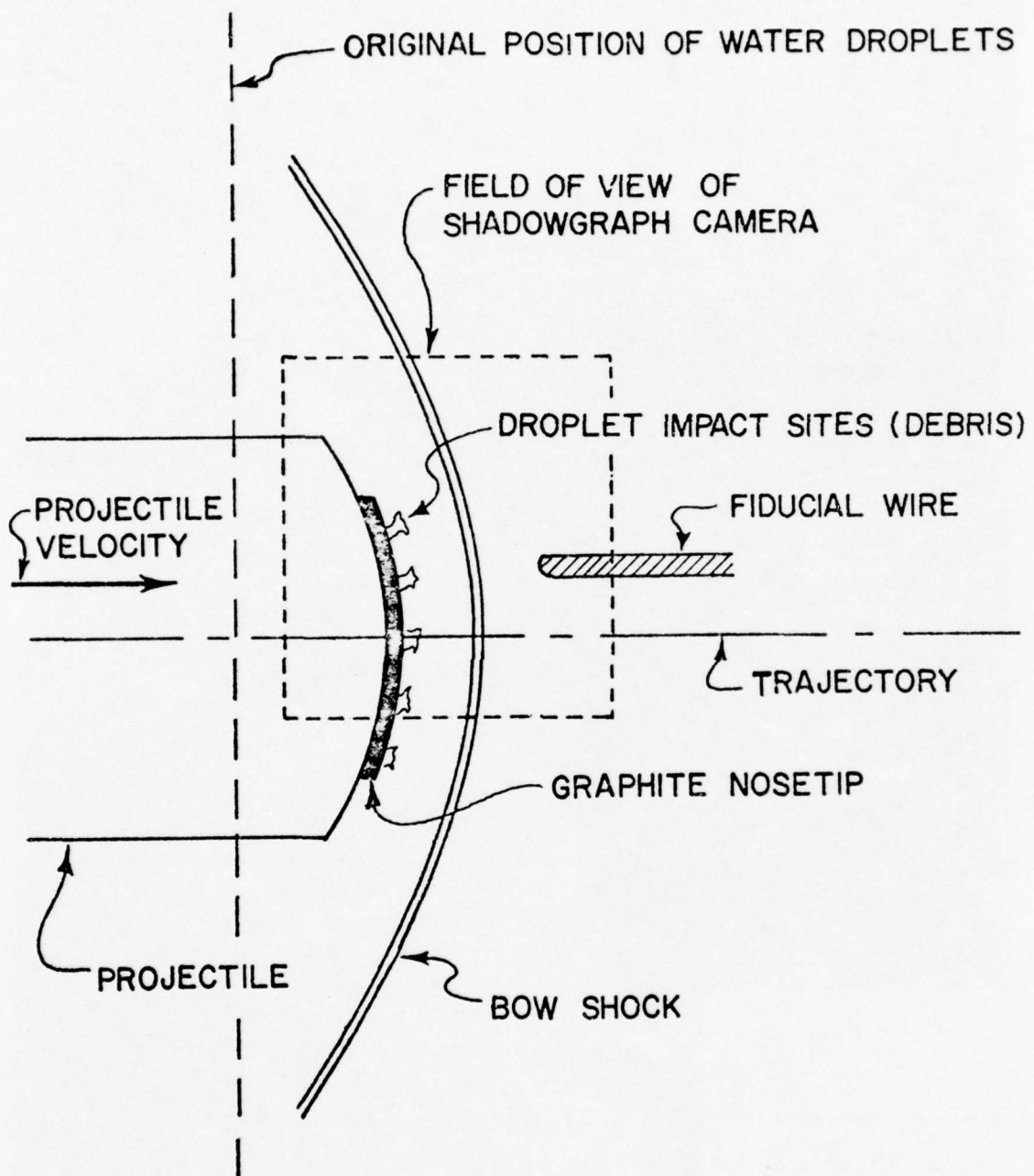


Figure 6. A schematic of the post-impact conditions as observed shadowgraphically.

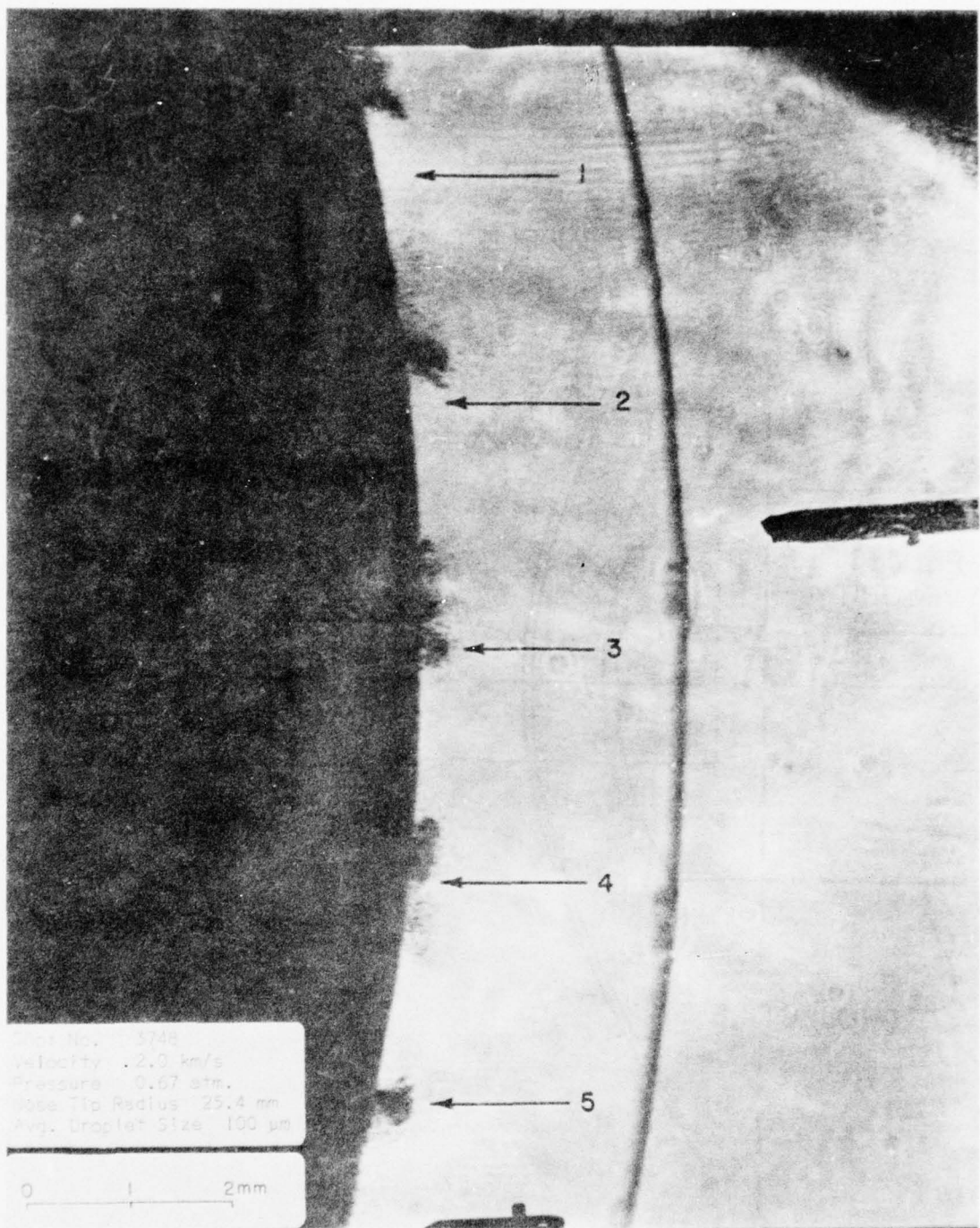


Figure 7. A typical droplet impact shadowgraph showing graphite impact debris.

carbide is extremely erosion resistant and any debris observed could reasonably be considered to be water. A shadowgraph of the impact is shown in Figure 8. There is quite clearly no debris generated at the impact sites. This is a marked contrast to the result for the similar impact on ATJS graphite shown in Figure 6. It was therefore concluded that there is no significant water contribution in the observed debris plumes.

The nondimensional time at impact, T_i , was calculated from the stand-off distance, Δ , at the impact point for each drop as follows:

$$T_i = \frac{\Delta}{D_o} \frac{\rho_2}{\rho_l}^{1/2} \quad (12)$$

where ρ_2 was the air density in the shock layer derived from normal shock relations in real air at the measured Mach number, and, D_o , the initial drop diameter, was measured from a preimpact shadowgraph. The Weber number for each drop was calculated from Equation (1).

4.2.1 90 - 100 μm Diameter Droplet Impacts

The data for all the impacts obtained on 90 - 100 μm droplets are collected in Table 2. The important reduced parameters are the Weber number and the nondimensional time at impact. The observation of impact debris is indicated for each droplet.

The data are presented graphically in Figure 9 which shows the nondimensional time at impact plotted as the Weber number for each observable drop. Each cluster of points originates from a particular shot. The closed symbols represent impacts in which impact debris was clearly observed, the open symbols signify no detectable debris at the impact site, and the half-closed symbols denote impacts in which debris, if present, is only just detectable. The cross shown in the figure represents typical error bars for time and Weber number.

The solid line represents the breakup time obtained from previous correlations⁽¹⁾ and is given by Equation (11).

$$T_b Q_m^{1/2} = 35 We^{-1/4} \quad (13)$$

For these shots the Mach number varied from six to about 53n. Over this range of Mach numbers Q_m is relatively constant and, from Reinecke, et al.,⁽¹⁾ has a value of:

$$Q_m \approx 0.8. \quad (14)$$

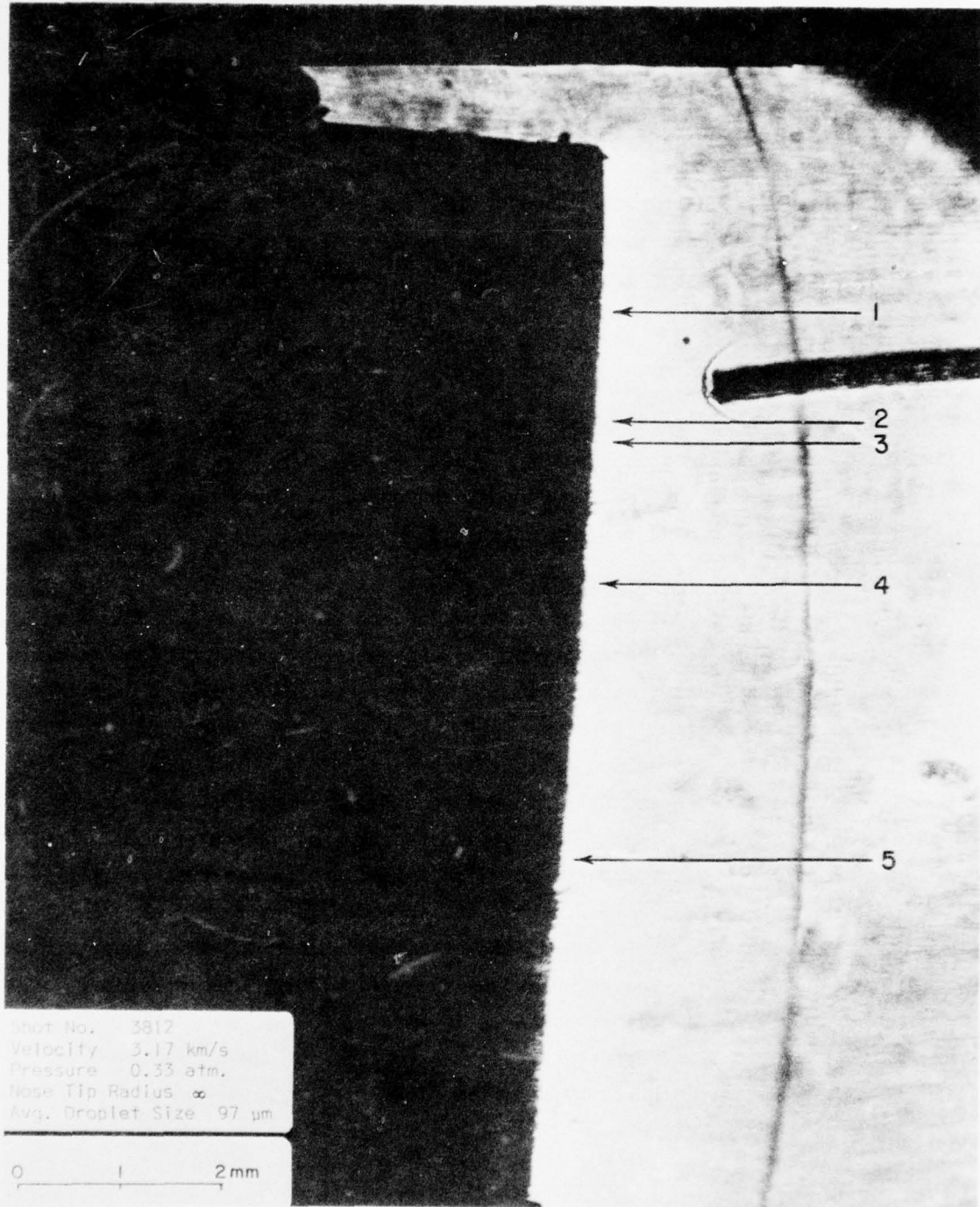


Figure 8. A shadowgraph of an impact on tungsten carbide.

TABLE 2. 90-100 μm DIAMETER WATER DROPLET IMPACTS

Shot No.	R_N (cm)	P_1 (atm)	V (cm/s)	Mach No.	ρ_d/ρ_1	ρ_2/ρ_1 (kg/m^3)	$\sqrt{\rho_2/\rho_d}$	Drop No.	U_0 (μm)	Weber No.	$x(\text{impact})$ (cm)	$T(\text{impact})$	Dribis
3744	25.4	0.67	3.75	10.8	9.1	7.3	8.54×10^{-2}	1	98	1.51 _{1.2}	1.82	1.59	yes
								2	96	1.51 _{1.4}	1.82	1.62	yes
								3	98	1.51 _{1.2}	1.82	1.62	yes
								4	98	1.51 _{1.2}	1.88	1.64	yes
								5	98	1.51 _{1.2}	1.93	1.68	yes
								Avg.	98				
3745	25.4	0.67	2.16	6.3	6.9	5.5	7.42×10^{-2}	1	102	37.0	2.68	1.95	yes
								2	100	36.3	2.66	1.97	yes
								3	100	36.3	2.70	2.00	yes
								4	100*	36.3	2.76	2.05	yes
								5	100*	36.3	2.80	2.08	yes
								Avg.	100				
3749	25.4	0.67	2.70	7.8	7.2	5.8	7.62×10^{-2}	1	103	60.5	2.81	2.08	yes
								2	98	57.6	2.66	2.07	yes
								3	98	57.6	2.60	2.02	yes
								4	99	58.1	2.60	2.00	yes
								5	99	58.1	2.76	2.12	yes
								Avg.	100				
3750	∞	0.67	2.90	8.4	7.5	6.0	7.75×10^{-2}	1	102	71.5	3.75	2.85	?
								2	98	68.7	3.93	3.11	no
								3	98	68.7	4.01	3.17	no
								4	95	66.6	4.01	3.27	no
								5	98*	68.7	3.91	3.09	no
								6	98*	68.7	3.80	3.00	?
								Avg.	98				
3752	∞	0.33	2.99	8.7	7.9	3.1	5.57×10^{-2}	1	85	32.7	3.54	2.32	yes
								2	82	31.6	3.80	2.58	yes
								3	87	33.5	3.75	2.40	yes
								Avg.	85				
3762	∞	0.50	2.85	8.3	7.5	4.5	6.71×10^{-2}	1	110	55.8	3.62	2.21	yes
								2	110	55.8	3.83	2.34	yes
								3	111	56.3	3.78	2.28	yes
								Avg.	110				
3768	25.4	0.33	3.93	11.4	9.1	3.6	6.00×10^{-2}	1	90	69.5	1.61	1.07	yes
								2	93	71.8	1.77	1.14	yes
								3	91	70.3	1.60	1.05	yes
								Avg.	91				
3769	∞	0.67	2.75	8.0	7.3	5.9	7.68×10^{-2}	1	100	62.6	3.21	2.47	yes
								2	101	62.6	3.48	2.65	?
								3	102	63.2	3.59	2.71	?
								Avg.	101				
3775	25.4	0.50	3.92	11.4	9.0	5.4	7.35×10^{-2}	1	75*	86.4	1.71	1.66	yes
								2	75*	86.4	1.76	1.71	yes
								3	75*	86.4	1.76	1.71	yes
								4	75*	86.4	1.81	1.76	yes
								5	75*	86.4	1.65	1.61	yes
								Avg.	75				
3812**	∞	0.33	3.17	9.2	8.1	3.2	5.66×10^{-2}	1	95	42.4	1.97	1.18	no
								2	93	41.5	2.16	1.32	no
								3	97	43.3	2.18	1.28	no
								4	100	44.7	2.31	1.32	no
								5	101	45.1	2.48	1.40	no
								Avg.	97				

 R_N nose tip radius P_1 range pressure V projectile velocity P_1 air density in range P_2 air density behind shock ρ_d droplet density d_0 droplet initial diameter x distance from shock front to impact T nondimensional time at impact

* droplet diameter not measurable, average used

** tungsten carbide projectile

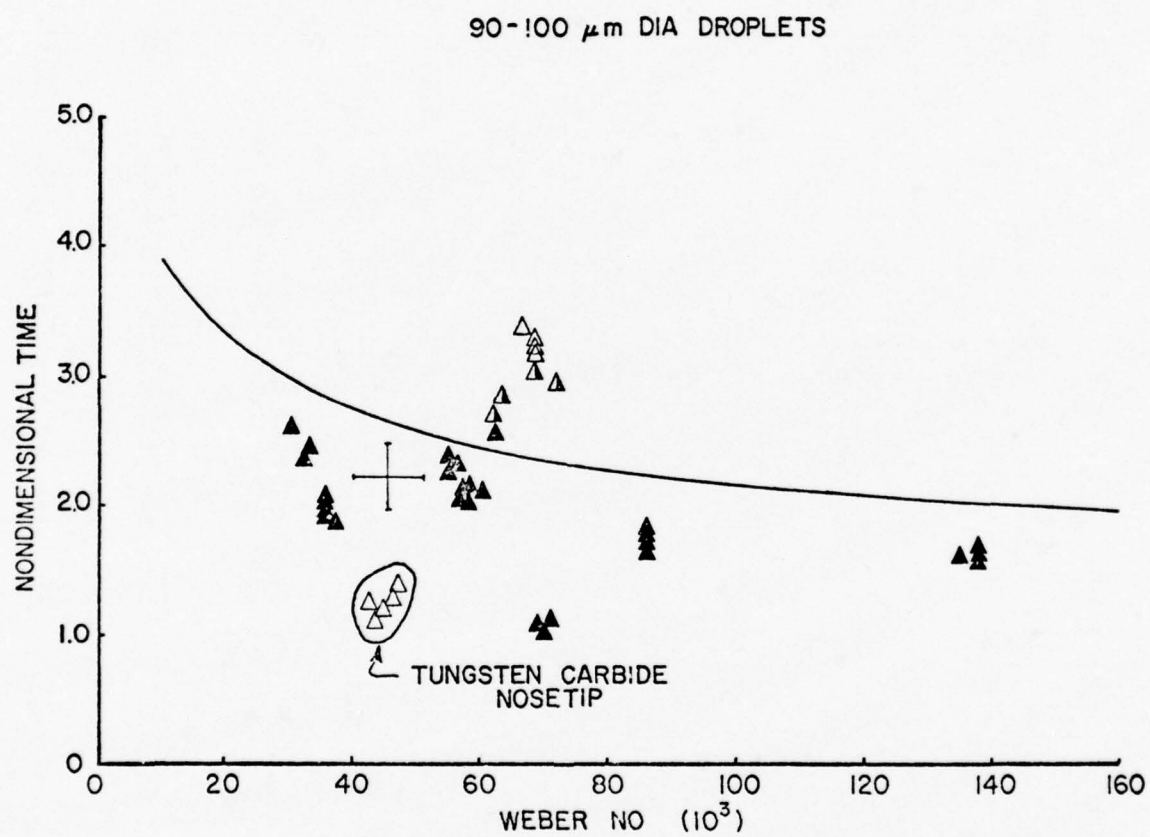


Figure 9. The nondimensional time at impact versus Weber number for 95 - 100 μm diameter droplets. The solid symbols indicate impacts in which debris was generated and the open symbols indicate impacts in which no debris was observed.

Substitution into Equation (13) provides:

$$T_b = 39We^{-1/4}, \quad (15)$$

and this is plotted in Figure 9.

The data show a region in which impact debris is definitely observed and erosion occurs, a transition region, and a region where debris is definitely not observed. The correlative breakup time falls in the transition region within the uncertainty in the correlation and the data.

4.2.2 35 - 40 μm Diameter Droplet Impacts

A shadowgraph of a typical 35 - 40 μm diameter droplet impact which produced debris is shown in Figure 10. A shadowgraph from a shot which did not produce debris is shown in Figure 11.

The data for all the impacts on 35 - 40 μm diameter droplets are collected in Table 3. The Weber numbers for nondimensional time at impact were calculated for each droplet and recorded in the table. In addition, the observation of impact debris is noted.

The data are presented graphically in Figure 12 which shows nondimensional time at impact plotted versus the Weber number for each observable droplet. The closed symbols represent impacts in which impact debris was observed, the open symbols signify no detectable debris at the impact site and the half closed symbols denote impacts in which debris, if present, is only marginally detectable.

The solid line represents the breakup time obtained from previous correlations as described for 90 - 100 μm diameter droplets. The range of Mach numbers was the same for the 35 - 40 μm diameter droplets as it was for the 90 - 100 μm diameter droplets, so the correlation is identical;

$$T_b = 39We^{-1/4}. \quad (16)$$

The nondimensional time to breakup is predicted to depend only on Weber numbers, and not explicitly on droplet diameter.

The data show a region in which debris is clearly observed, a transition region and a region in which debris is not observed. The predicted breakup time falls in within the transition zone the uncertainty in the correlation and the data.



Figure 10. A shadowgraph showing impact debris produced by the impact of 35 - 40 μm diameter droplets on ATJS graphite.

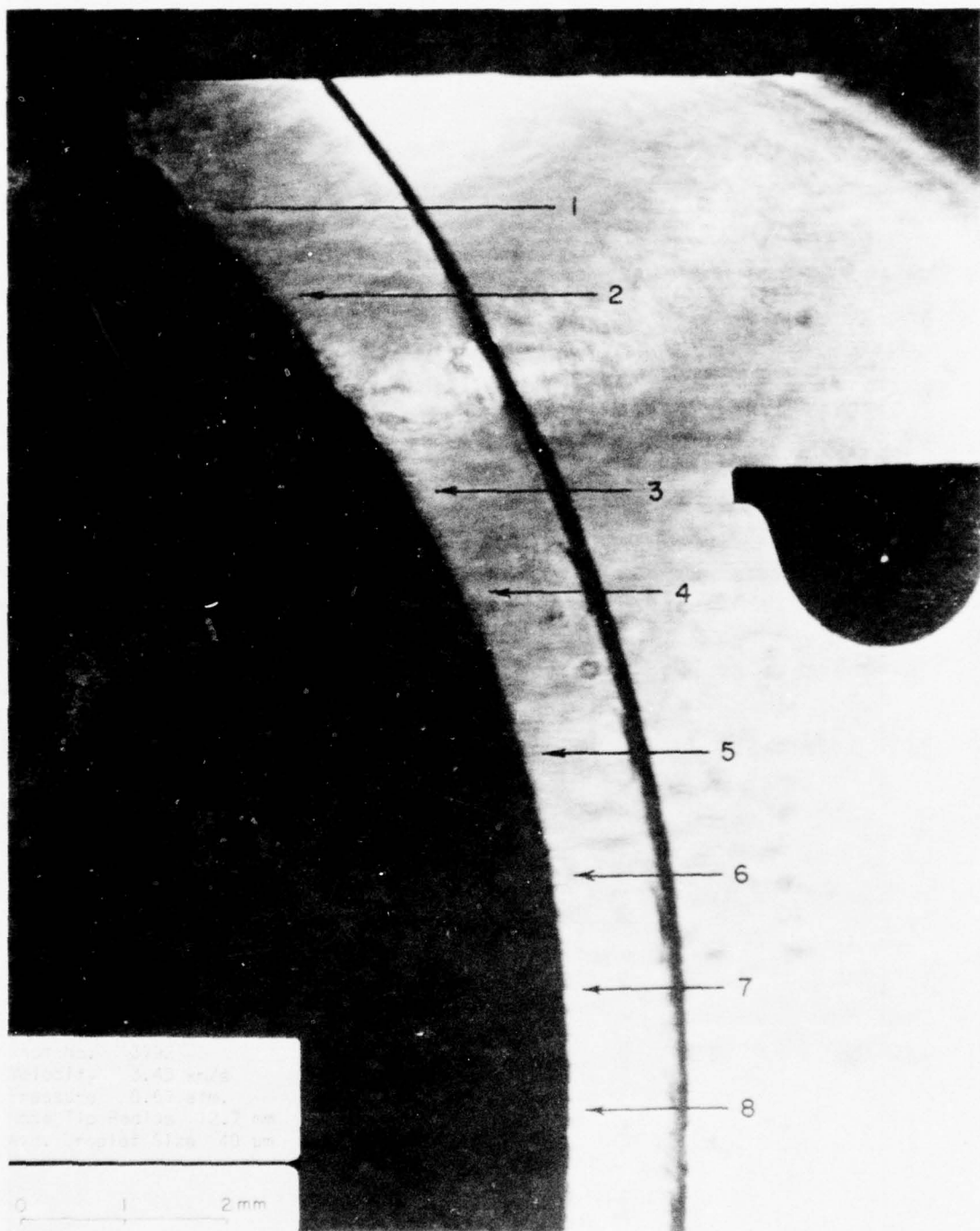


Figure 11. A shadowgraph showing no impact debris on ATJS graphite after encounter with 35 - 40 μm diameter droplets.

TABLE 3. 35-40 μm DIAMETER WATER DROPLET IMPACTS

nose tip radius
 range pressure
 projectile velocity
 air density in range
 air density behind shock

P_d droplet density D_0 droplet initial diameter x distance from shock front to impact t nondimensional time at impact * droplet diameter not measurable, average used

35-40 μm DIA DROPLETS

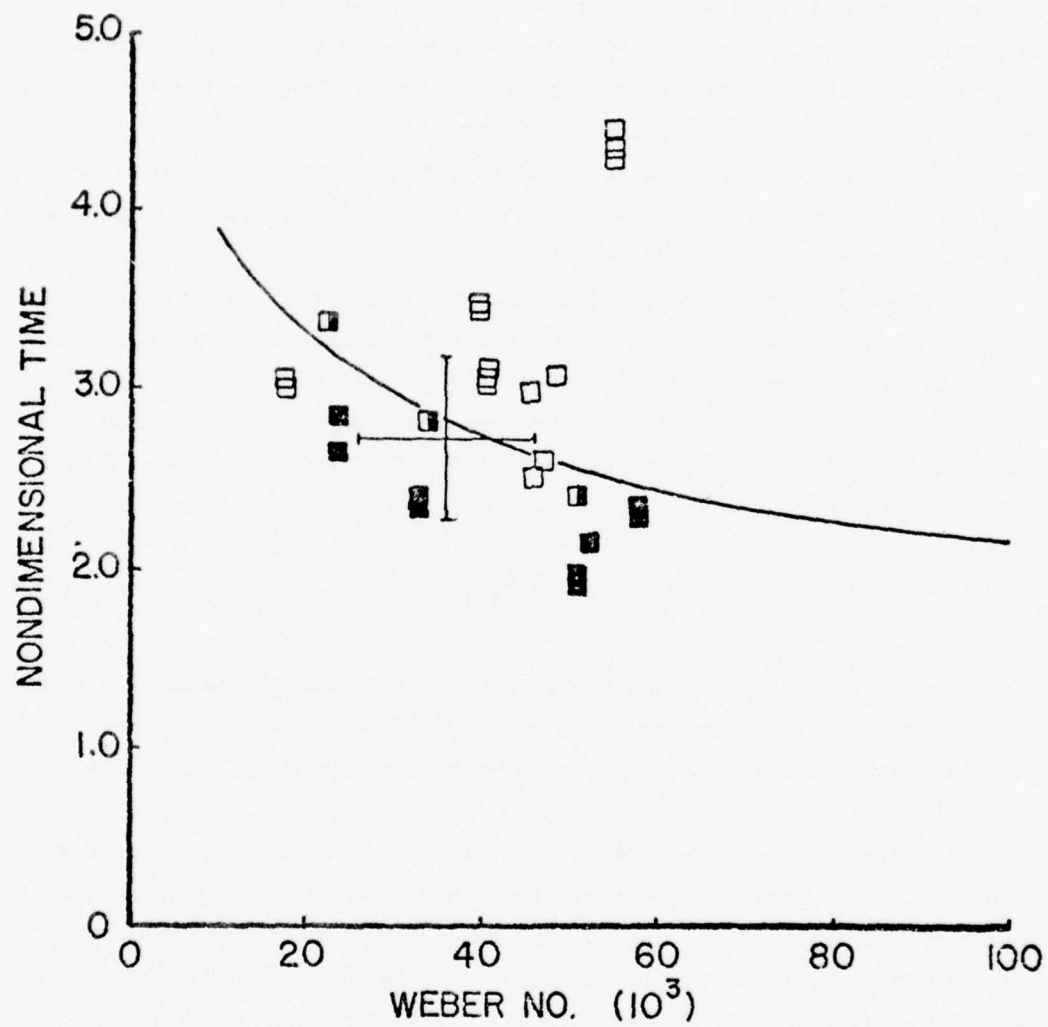


Figure 12. The nondimensional time at impact versus Weber number for 35 - 40 μm diameter droplets. The open symbols represent impacts in which no debris was observed. The closed symbols represent impacts in which debris was observed and the half-closed symbols represent impacts in which debris was only marginally detectable.

4.2.3 25 - 30 μm Diameter Droplet Impacts

Three data shots onto 25 - 30 μm diameter droplets were obtained. A typical shadowgraph is shown in Figure 13. Because of the small droplet diameter, the standoff distance of the bow shock had to be reduced to low values to obtain nondimensional times at impact at which impact debris might be expected. The nosetip radius was reduced to approximately 9 mm and the velocity was increased to above 4.5 km/s. Despite these efforts, no debris producing impacts were observed.

The data for all the shots on 25 - 30 μm diameter droplets are collected in Table 4. Weber number and nondimensional time at impact were calculated for each droplet.

The data are presented graphically in Figure 14 which shows the nondimensional time at impact versus the Weber number for each observable droplet. In no case was debris positively identified.

The solid line indicates the predicted droplet breakup time from correlations⁽¹⁾ and is identical to that for 35 - 40 μm and 90 - 100 μm diameter droplets;

$$T_b = 39 \text{We}^{-1/4}. \quad (17)$$

The correlation predicts that debris should have been produced at a number of the impact sites. However, the uncertainties in the 25 - 30 μm diameter droplet data indicate the disagreement with the predicted value is not significant.

There were a number of experimental difficulties encountered with the 25 - 30 μm diameter droplets. The stream was not stable and tended to move about erratically in space. The exact position of the droplets at impact with respect to projectile trajectory was therefore not known very well. The impact of such small droplets might be expected to produce only small amounts of debris which would be difficult to detect. The magnitudes of a number of these factors will be examined in the following sections.

4.3 EXPERIMENTAL UNCERTAINTIES AND ERRORS

Droplet breakup and impact damage threats are characterized in terms of the nondimensional time at impact (T) and the Weber number (We). The effects of experimental and measurement errors in these quantities were examined.

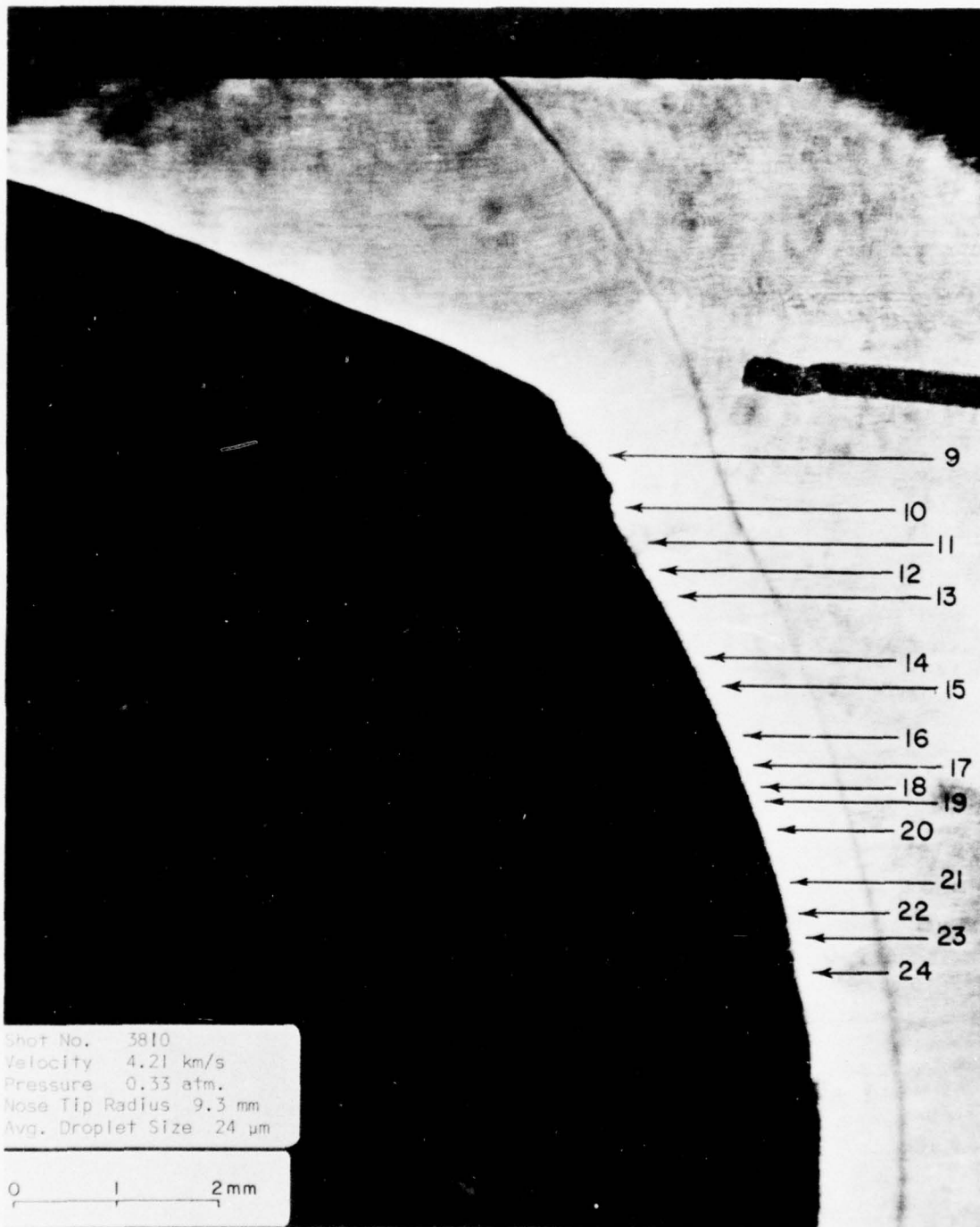


Figure 13. A shadowgraph of the encounter of an ATJS projectile with 25 - 30 μm droplets.

TABLE 4. 25-30 μm DIAMETER WATER DROPLET IMPACTS

Stat. No.	R_N (mm)	P_1 (atm)	V (km/s)	March No.	ρ_1/ρ_1	ρ_2/ρ_1 (kg/m ³)	$\sqrt{\rho_2/\rho_1}$	Droplet No.	D_0 (μm)	Water No. ($\times 10^3$)	$x(\text{impact})$ (nm)	$T(\text{impact})$	Droplets
3806	12.7	0.33	4.31	12.5	9.4	3.7	6.08×10^{-2}	10	24*	22.9	1.97	5.00	no
								11	24*	22.9	1.71	4.39	no
								12	24*	22.9	1.65	4.19	no
								13	24*	22.9	1.56	3.97	no
								14	24*	22.9	----	----	no
								15	24*	22.9	----	----	no
								16	24*	22.9	----	----	no
								17	24*	22.9	----	----	no
								18	24*	22.9	----	----	no
								19	24*	23.0	----	----	no
								20	24*	23.0	1.29	5.93	no
								21	24*	23.0	1.25	5.63	no
								22	24*	23.0	1.25	5.63	no
								23	24*	23.0	1.25	5.63	no
								24	24*	23.0	1.25	5.63	no
								25	24*	23.0	1.25	5.63	no
								Avg.	24	23.0	1.25	5.63	no
3807	9.9	0.33	4.48	13.0	9.5	3.8	6.16×10^{-2}	20	27*	29.0	2.24	5.14	no
								21	27*	29.0	2.19	5.03	no
								22	27*	29.0	2.11	4.85	no
								23	27*	29.0	2.09	4.80	no
								24	27*	29.0	2.04	4.68	no
								25	27*	29.0	2.01	4.62	no
								26	27*	29.0	1.96	4.50	no
								27	27*	29.0	1.90	4.36	no
								28	27*	29.0	1.90	4.36	no
								29	27*	29.0	1.86	4.27	no
								30	27*	29.0	1.85	4.25	no
								31	27*	29.0	1.84	4.13	no
								32	27*	29.0	1.80	4.13	no
								33	27*	29.0	1.80	4.13	no
								34	27*	29.0	1.79	4.11	no
								35	27*	29.0	1.78	4.08	no
								36	27*	29.0	1.78	4.08	no
								37	27*	29.0	1.76	4.04	no
								38	27*	29.0	1.76	4.04	no
								39	27*	29.0	1.76	4.04	no
								Avg.	27	29.0	1.76	4.04	no
3810	9.3	0.33	4.21	12.2	9.4	3.7	6.10×10^{-2}	9	24*	21.9	1.27	3.22	no
								10	24*	21.9	1.28	3.25	no
								11	24*	21.9	1.29	3.28	no
								12	24*	21.9	1.29	3.28	no
								13	24*	21.9	1.24	3.15	no
								14	24*	21.9	1.15	2.92	no
								15	24*	21.9	1.12	2.85	no
								16	24*	21.9	1.07	2.72	no
								17	24*	21.9	1.00	2.54	no
								18	24*	21.9	1.00	2.542	no
								19	24*	21.9	0.98	2.49	no
								20	24*	21.9	0.96	2.44	no
								21	24*	21.9	0.91	2.31	no
								22	24*	21.9	0.91	2.31	no
								23	24*	21.9	0.91	2.31	no
								24	24*	21.9	0.91	2.31	no
								Avg.	24	21.9	0.91	2.31	no

R_N nose tip radius
 P_1 range pressure
 V projectile velocity
 ρ_1 air density in range
 ρ_2 air density behind shock

ρ_d droplet density
 D_0 droplet initial diameter
 x distance from shock front to impact
 T nondimensional time at impact

* droplet diameter not measurable, average used

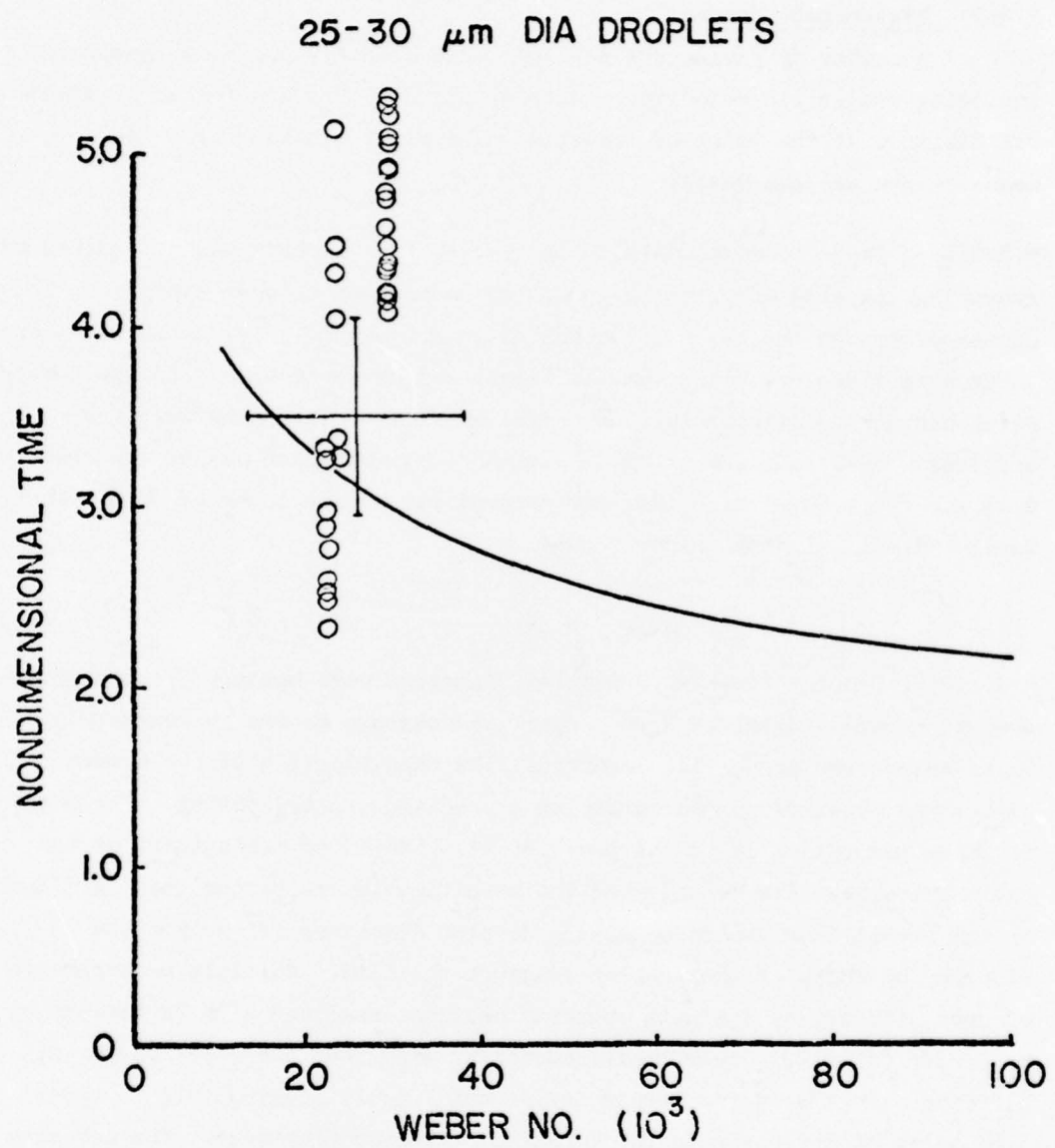


Figure 14. Non-dimensional time-at-impact versus Weber number for 25-30 μm diameter droplets.

In addition, the sensitivity of the shadowgraphic system to certain parameters for the detection of debris plumes was treated.

4.3.1 Measurement Errors

A number of parameters were measured directly for each impact including projectile velocity v , droplet diameter D_o , and the shock stand-off distance at the point of impact Δ . The error in each of these measurements was evaluated.

4.3.1.1 **Projectile Velocity.** The projectile velocity was determined by measuring the time of flight between two laser beam trigger stations. The distance between the laser beams was 25 cm and was measured to ± 0.1 cm (one laser beam diameter). The time of flight was measured with a 10 mHz counter which had a resolution of 0.1 μ s. Typical time of flight between the stations was 70 μ s. The error in distance determination was of the order of 0.4% and the error in the time measurement was of the order of 0.1%. Therefore, the error in the velocity was:

$$\delta v/v = 0.5\%. \quad (18)$$

4.3.1.2 **Droplet Diameter.** Droplet diameters were measured from a photographic negative obtained from a spark shadowgraph camera approximately 50 μ s before the projectile impacted. The magnification of the camera system was obtained by photographing a precision Ronchi ruling. The magnification was typically of the order of 9:1. Repeated measurement of the calibration negative established the magnification to better than 1%. Most of the errors involved in measuring droplet diameters arise from the blurring of edges of the droplet image on the film. Multiple measurements of drop diameter by a single operator produced readings with variations of the order of 2%. However, measurements by different operators and/or at different times produced larger deviations largely attributable to the difficulty of interpreting the location of the droplet edge. The accuracy of the measurement of droplet diameters was therefore determined largely by the quality of the camera optics and the film resolution. Assuming the film/camera system was approximately 20 lines/mm, the resolution in droplet diameter would be $\pm 5 \mu\text{m}$. This was consistent with the observations of measurement variation in droplet diameter. The error in droplet diameter was therefore:

$$\delta D_o = 5 \mu\text{m}, \quad (19)$$

independent of droplet diameter.

4.3.1.3 Shock Standoff Distance. The nondimensional time at impact is related to the shock standoff distance at the impact location. The shock standoff distance was measured from the laser/microscope camera photographs. The magnification of the camera system was obtained by photographing a precision Ronchi ruling and measuring the ruling spacing on the photograph. Repeated measurement of the magnification indicated an accuracy of the order of 0.5%. The magnification was typically 20:1.

Standoff distances were typically of the order of 1 mm and appeared on the film as 20 mm. The distances on the film could readily be measured to within 0.5 mm. The accuracy of shock standoff distance measurements was therefore considered to be the sum of the magnification and measurement errors;

$$\frac{\delta \Delta}{\Delta} \approx 3\%. \quad (20)$$

4.3.2 Derived Parameters

A number of parameters were derived from primary data or obtained from handbooks, including Mach number, air density, droplet density and droplet surface tension. Possible errors in each of these parameters were evaluated.

4.3.2.1 Mach Number. The Mach number was obtained by dividing the projectile velocity by the sound speed of the air. The sound speed of air was obtained from the Handbook of Applied Engineering Science⁽⁶⁾ for a temperature of 295°K was 344 m/s. The range was partially evacuated for each shot, however, sound speed is independent of pressure over the range tested (0.33 to 0.67 atm). The range was evacuated at constant temperature; however, room temperature varied erratically between about 290°K and 300°K. The resulting sound velocities varied from 341 m/s to 347 m/s. This uncertainty together with the error in velocity measurement results in an error of the Mach number of:

$$\frac{\delta M}{M} \approx 1.5\%. \quad (21)$$

⁽⁶⁾Handbook of Applied Engineering Science, 1st Edition, Chemical Rubber Company, Cleveland, 1970.

4.3.2.2 Shock Layer Air Density. The air density ratio across the projectile shock was obtained from charts for imperfect air contained in Reference 7. These charts account for both Mach number and free-stream pressure. The reading accuracy from the chart was estimated to be of the order of 1%. The error in Mach number must be added to this, so the total error in density ratio is estimated to be 1.5%.

Errors in shock layer density also arise from errors in free-stream density. The free-stream density is calculated from ambient density using the measured range pressure. The ambient density varies with ambient temperature, which varied from 290°K to 300°K. The resulting variation of ambient density extended from 1.22 kg/m^3 to 1.18 kg/m^3 -- about 2% from the value of 1.20 which was used for calculations.

The range was evacuated at constant temperature. The range pressure was measured, and the free-stream density was calculated from the ambient pressure and density. Errors in range pressure measurement are therefore reflected in the free-stream density. The pressure was measured to 0.01 atm, resulting in an error of about 2% for a mean value of 0.5 atm. The shock density ratio also varied with shock angle. The shock front was normal only near the stagnation region of the projectile. Away from the stagnation region the shock became oblique but remained strong. The maximum shock angle observed in the impact region was about 15°. The effect of this obliquity on air density outside the stagnation region was not estimated. These errors all add, to provide maximum estimated error in the shock layer density of

$$\delta \rho_2 / \rho_2 = 4.5\%. \quad (22)$$

4.3.2.3 Droplet Density. The droplet density was taken as 1000 kg/m^3 , the density of water at room temperature. The error in this value was regarded to be negligible.

4.3.2.4 Droplet Surface Tension. The surface tension of water was obtained from the Handbook⁶ and at 295°K is 0.0725 N/m. Over the range of ambient temperatures (290-300°K), the surface tension varied from 0.0732 to 0.0717 N/m, a deviation of:

$$\delta \sigma_l / \sigma_l = 1\%. \quad (23)$$

⁷Lewis, H. and Burgess, E. G., "Charts of Normal Shock Properties in Imperfect Air", AEDC-TDR-64-43, 1964.

Distilled water was employed so the effects of impurities on surface tension are probably negligible.

4.3.3 Errors of Reduced Data

The primary and derived data errors collected from the preceding paragraphs are tabulated in Table 5. The cumulative effects of these errors on the reduced quantities of Weber number and nondimensional time were then determined by adding the appropriate values from Table 5. The results are displayed in Table 6.

Typical error bars are shown in Figures 9, 12, and 14. The correlative prediction of droplet breakup clearly lies within the uncertainty in the data.

4.3.4 Observation Uncertainties

There was a condition under which impacts could occur and debris, although present, could not be detected. If the impacts occurred beyond the "horizon" of a spherical nosetip, the impact site became unobservable to the shadowgraphic camera. The conditions are illustrated in Figure 15. In order to observe the impact debris, the debris plume must be longer than the shielded distance.

The shielded distance, x , is a function of the off-center displacement, y , of the droplets at impact, and may be expressed in terms of the nosetip radius, R_N , as:

$$x = R_N - (R_N^2 - y^2)^{1/2} \quad (24)$$

Four nosetip radii were used; 9.1 mm, 12.7 mm, 25.4 mm and ∞ (flat). The shielded distance versus off-center displacement is shown plotted in Figure 16. For the flat nosetips the shielded distance given by Equation (24) is zero.

4.3.4.1 Off-Center Displacements. There are two sources of off-center displacements: projectile fly-off and droplet stream placement. The droplets were located with respect to a fiducial wire which was accurately located to less than 0.5 mm from trajectory. The 90 - 100 μm and 35 - 40 μm diameter droplet streams were stable and remained in the set location indefinitely. The 25 - 30 μm diameter stream was relatively unstable, and moved erratically around the set position up to 1 mm off trajectory.

TABLE 5. ESTIMATED DATA ERRORS

Parameter	Estimated Error (%)
velocity (v)	0.5
droplet diameter (D_o):	
90-100 μm diameter	5.0
35-40 μm diameter	13.5
25-30 μm diameter	18.5
shock standoff (Δ)	3.0
shock layer density	4.5
droplet surface tension	1.0

TABLE 6. ESTIMATED ERRORS IN REDUCED DATA

Droplet Diameter	Error (%)	
	Weber Number	Nondimensional Time
	We	T
90-100 μm	11.5	10.2
35-40 μm	20.0	18.2
25-30 μm	25.0	23.2

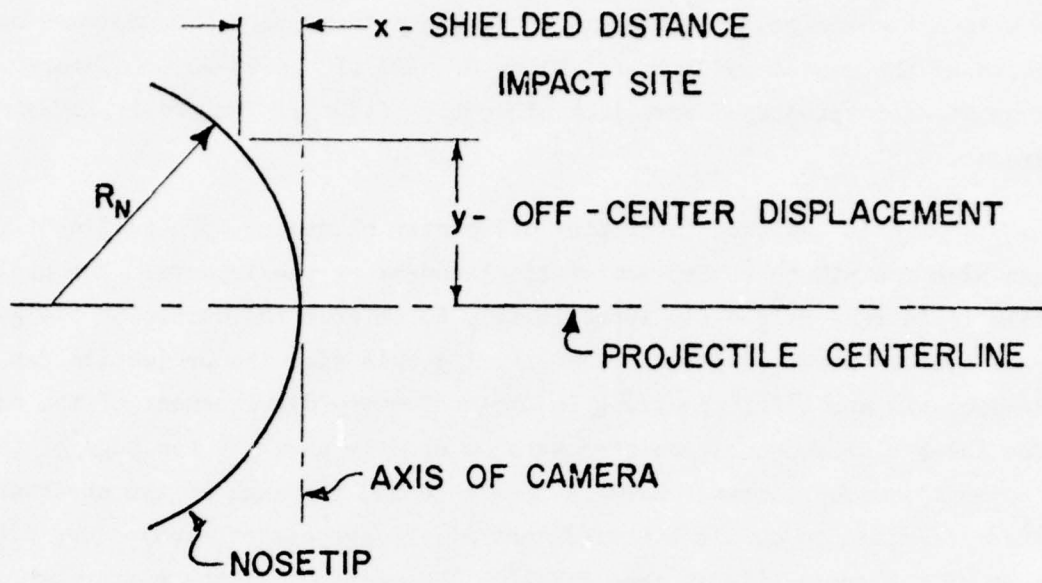


Figure 15. The geometry of off-center impacts.

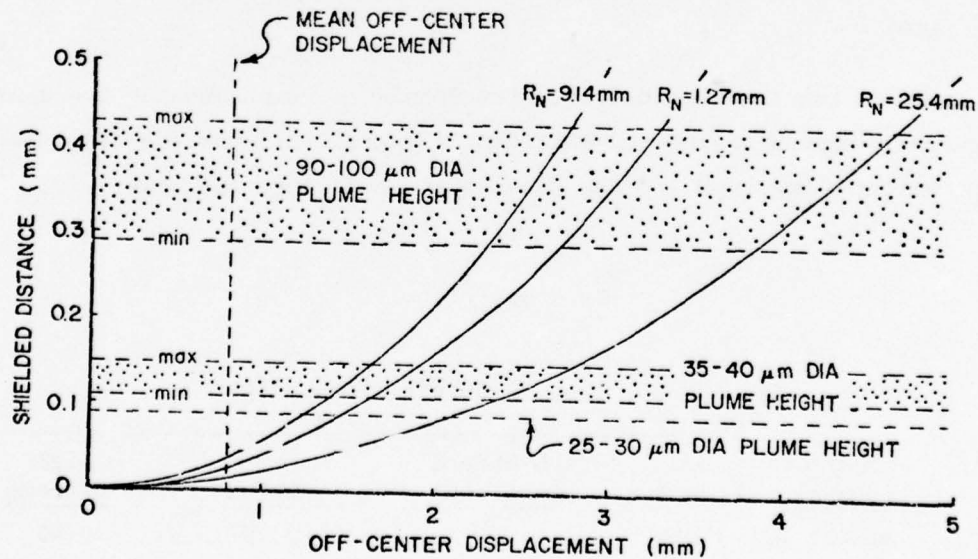


Figure 16. Shielded distance and debris plume height versus off-center displacement.

The only indication of the stream position at impact is obtained from the pre-impact shadowgraph. Droplets grossly off trajectory (~ 1 mm) were out of focus of the camera and appeared blurred. All of the 25-30 μm diameter droplet shots displayed some lack of droplet focus in the pre-impact shadowgraphs.

In addition to droplet off-center placement, projectile "flyoff" can also contribute to off-center displacement of the impacts. The projectile is in free flight for approximately 50 cm from the muzzle of the guide rail system to the droplet stream. During this time the projectile can develop yaw and lift, resulting in off-trajectory displacement of the nosetip. The laser-microscope camera shadowgraphs usually show the top edge of the projectile. The distance between this edge and the edge of the shadowgraph was determined to obtain a measurement of the average off-trajectory displacement of the projectile in free flight. The mean of all the measurements was taken as the trajectory. The standard deviation was assumed to be a measurement of the mean off-trajectory displacement (in any direction). The mean was found to be 0.3 mm.

The total off-center displacement of the impact sites could therefore be as much as 0.8 mm on the average. These values are indicated on Figure 16.

4.3.4.2 Debris Plume Height. For debris to be observable the debris plume must extend beyond the shielded distance. All the debris plumes observed were measured and the results are collected in Table 7.

TABLE 7

Debris Plume Heights
(mm)

Droplet Diameter	Mean	Standard Deviation	Low Extreme	High Extreme
90-100 μm	0.36	.02	0.29	0.43
35-40 μm	0.13	.01	0.11	0.15
25-30 μm	--	--	00	00

No debris plumes were clearly observed on 25-30 μm diameter droplet impacts.

However, the plume heights appear to scale approximately as the droplet diameter so the 25-30 μm diameter droplet debris plumes might be assumed to be of the order of 0.09 mm high. These values are all indicated on Figure 16.

The 35-40 μm and 90-100 μm diameter droplet testing was conducted on nosetip 12.7 mm in radius or greater. From Figure 16 it is apparent that debris should have definitely been observable for these sizes.

The 25-30 μm diameter droplets were tested on 9.1 mm radius nosetips. In addition, the erratic motion of the drop stream introduces an uncertainty into the off-center displacement of the water drops. The number of tests conducted on 25-30 μm diameter drops was not sufficient to reliably locate the breakup criterion.

SECTION V
CONCLUSIONS

Observations of the dilatation and breakup of 90-100 μm diameter droplets just prior to impact indicated that the droplets behave as observed in shock tubes. For the Weber numbers investigated ($>20,000$), the breakup mode was the catastrophic instability. The growth of unstable surface waves in the droplets leading face could be readily observed. Droplet dilatation was measured and agreed very well with the data of Reinecke, et al.⁽¹⁾ (See Figure 5).

The impact of water droplets which survive transit through the low shock layer was observed. It was found that the observed debris generated at impact on ATJS graphite was predominantly graphite. Therefore, the detection of debris may be used as a test for material damage. That is, if debris is observed at an impact site, an erosive impact occurred. If debris is not observed at an expected impact site, the droplet must have broken up prior to impact.

This determination of the breakup criterion was examined for 90-100 μm , 35-40 μm , and 25-30 μm diameter water droplets. It was found that over the range of Weber numbers tested (20,000 to 160,000), the breakup criteria found agreed, within the data uncertainty, with the correlation of Reinecke, et al.⁽¹⁾ The results are collected together in Figure 17. The uncertainty in the 25-30 μm diameter droplet data was so large that it does not correlate well with prediction. The 90-100 μm and 35-40 μm diameter droplet results show very good agreement.

The results presented in this report provide strong, direct confirmation of the breakup criteria at high Weber numbers ($>20,000$) derived from shock tube water droplet breakup observations. The study extended direct observation of the breakup criteria down to droplets of the order of 25 μm in diameter, thus including most of the mass contained in nonprecipitating clouds.

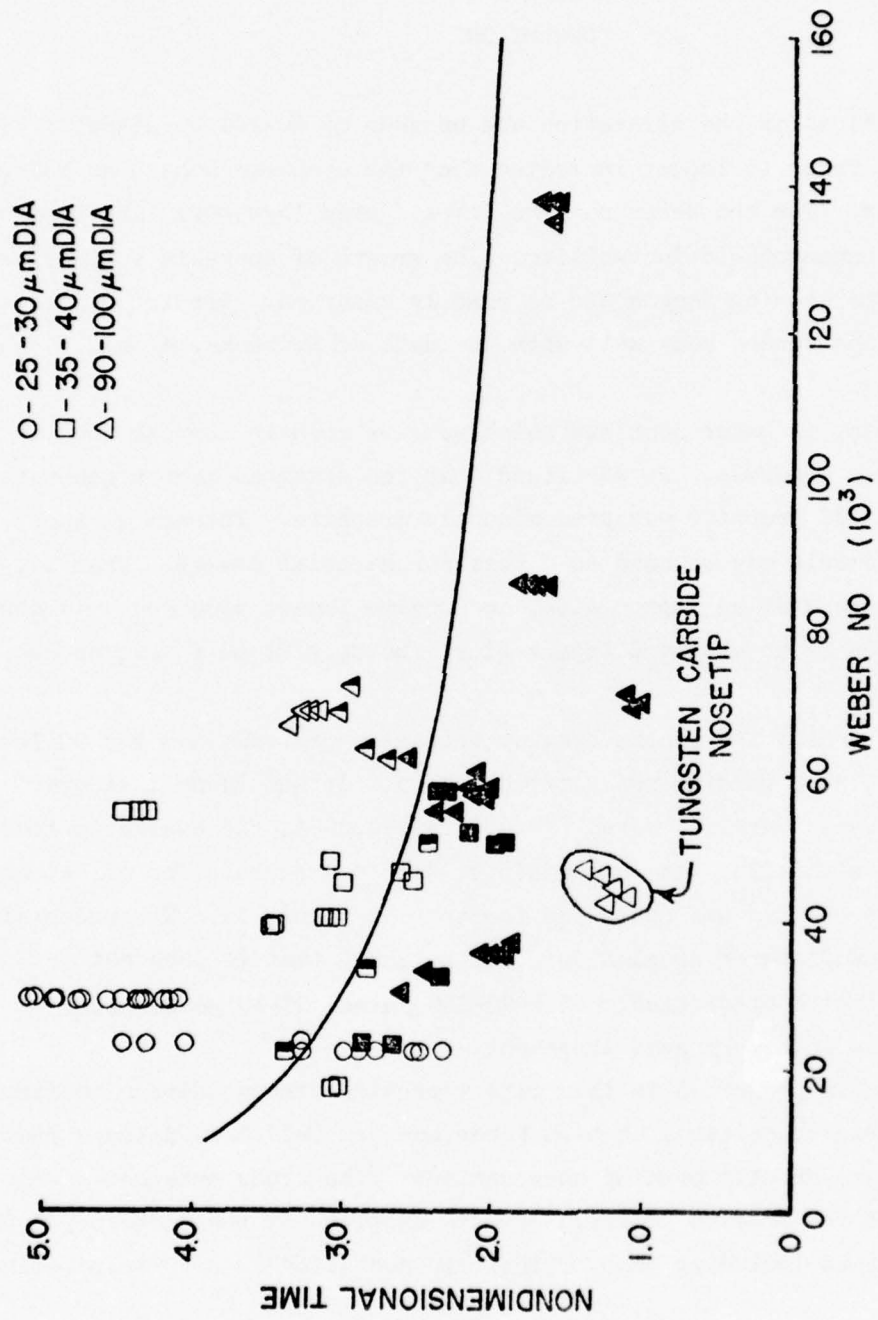


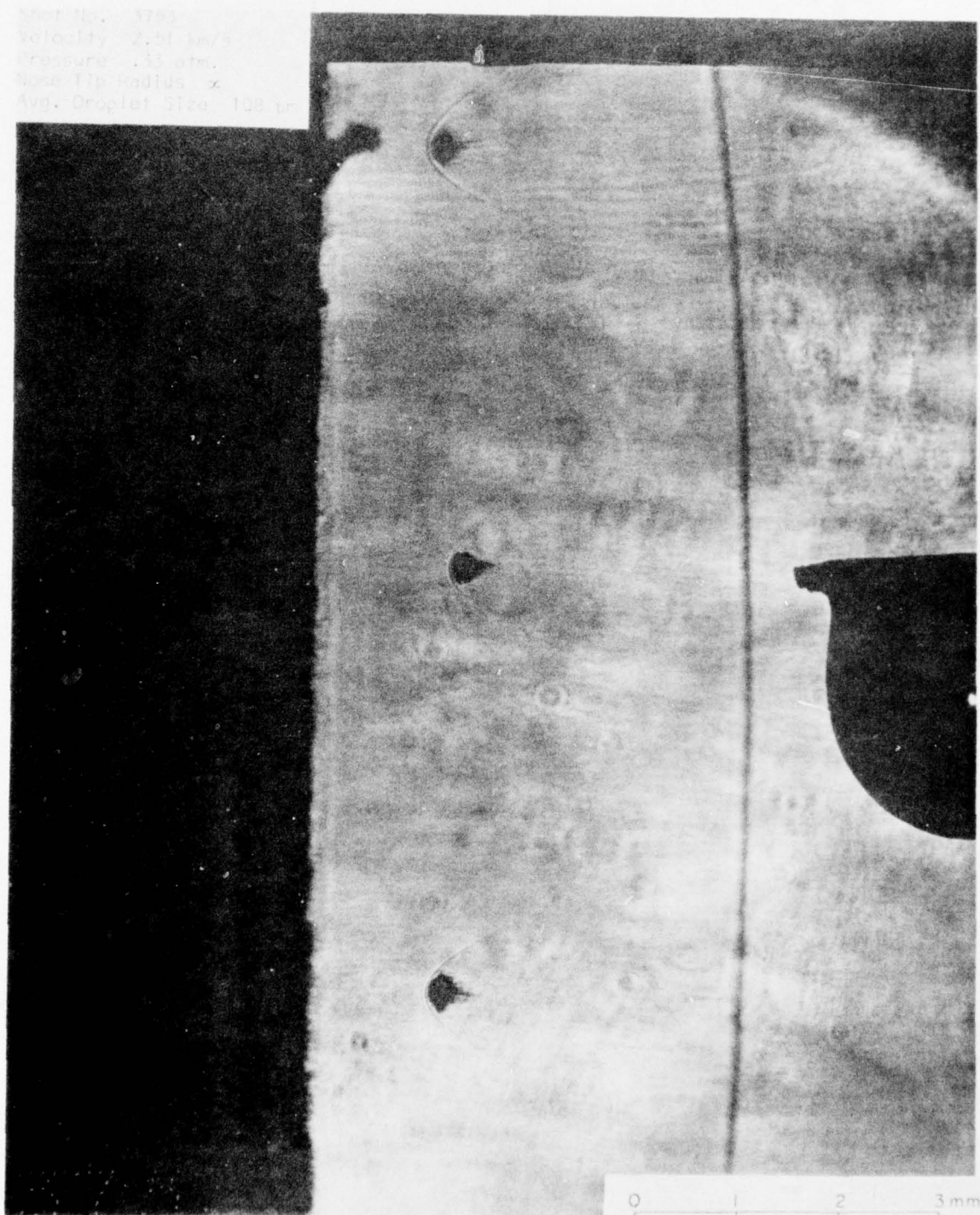
Figure 17. Nondimensional time at impact versus Weber number for all the data collected.

REFERENCES

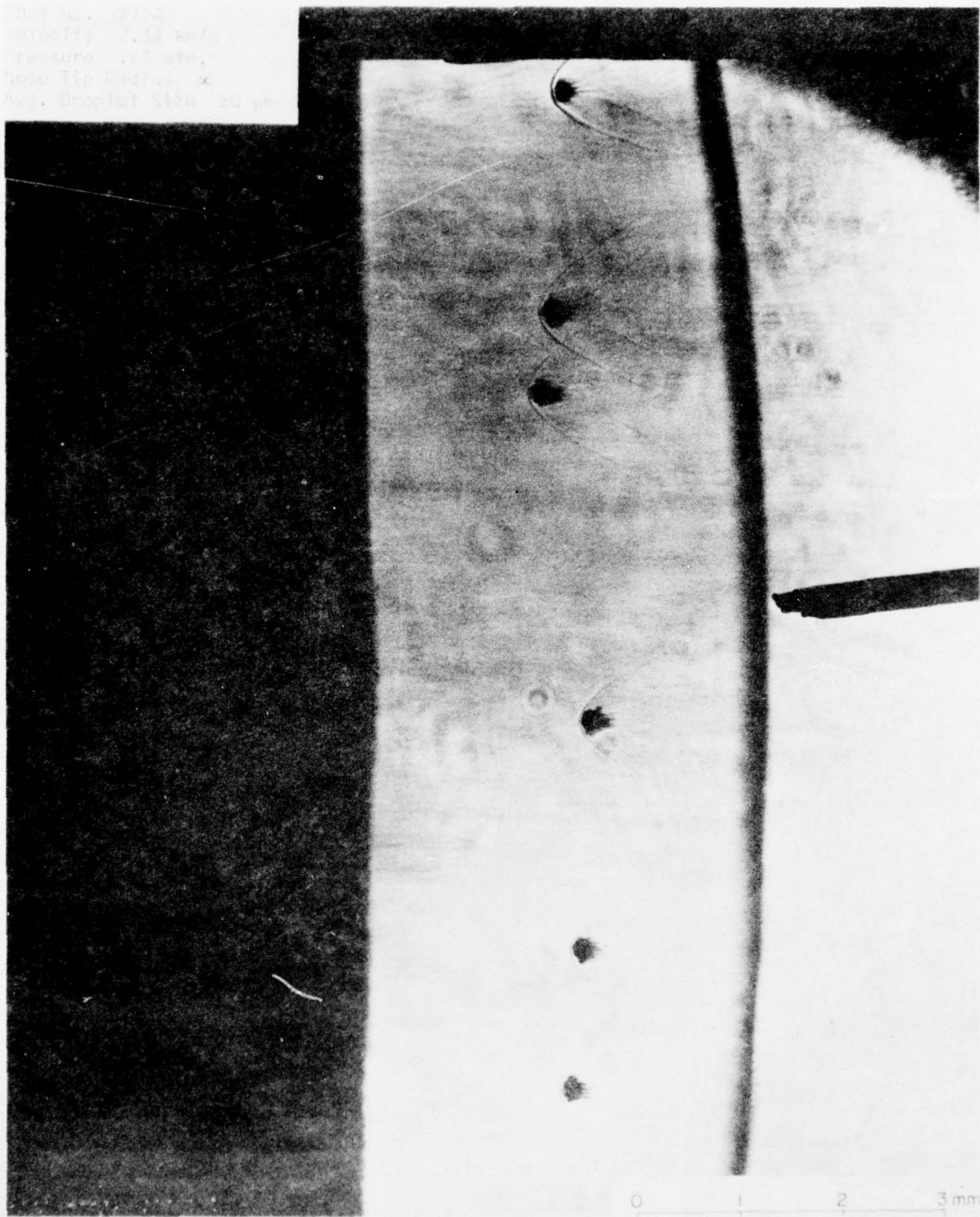
1. Reinecke, W. G., Waldman, G. D., McKay, W. L. and Ziering, M. B., "Shock Layer Shattering of Water Drops and Ice Crystals in Reentry Flight", AFML-TR-75-71.
2. Jaffe, N. A., "Hydrometer Shock Interactions", Interim Technical Report, Contract DNA001-74-C-0051.
3. Ranger, A. A. and Nichols, J. A., "Aerodynamic Shattering of Liquid Droplets", AIAA Journal, 7: 285-290, 1969.
4. Barber, J. P., Grood, E. S., Taylor, H. R. and Hopkins, A. K., "Water Drop/Bow Shock Interactions", AFML-TR-75-105.
5. Teng, R. N., Hickman, R. S. and Sutila, G. E., "Development of a Scaled-up Hypervelocity Projectile Guiding and Retrieving System", AEDC-TR-74-123.
6. Handbook of Applied Engineering Science, 1st Edition, Chemical Rubber Company, Cleveland, 1970.
7. Lewis, C. H. and Burgess, E. G., "Charts of Normal Shock Properties in Imperfect Air", AEDC-TDR-64-43, 1964.

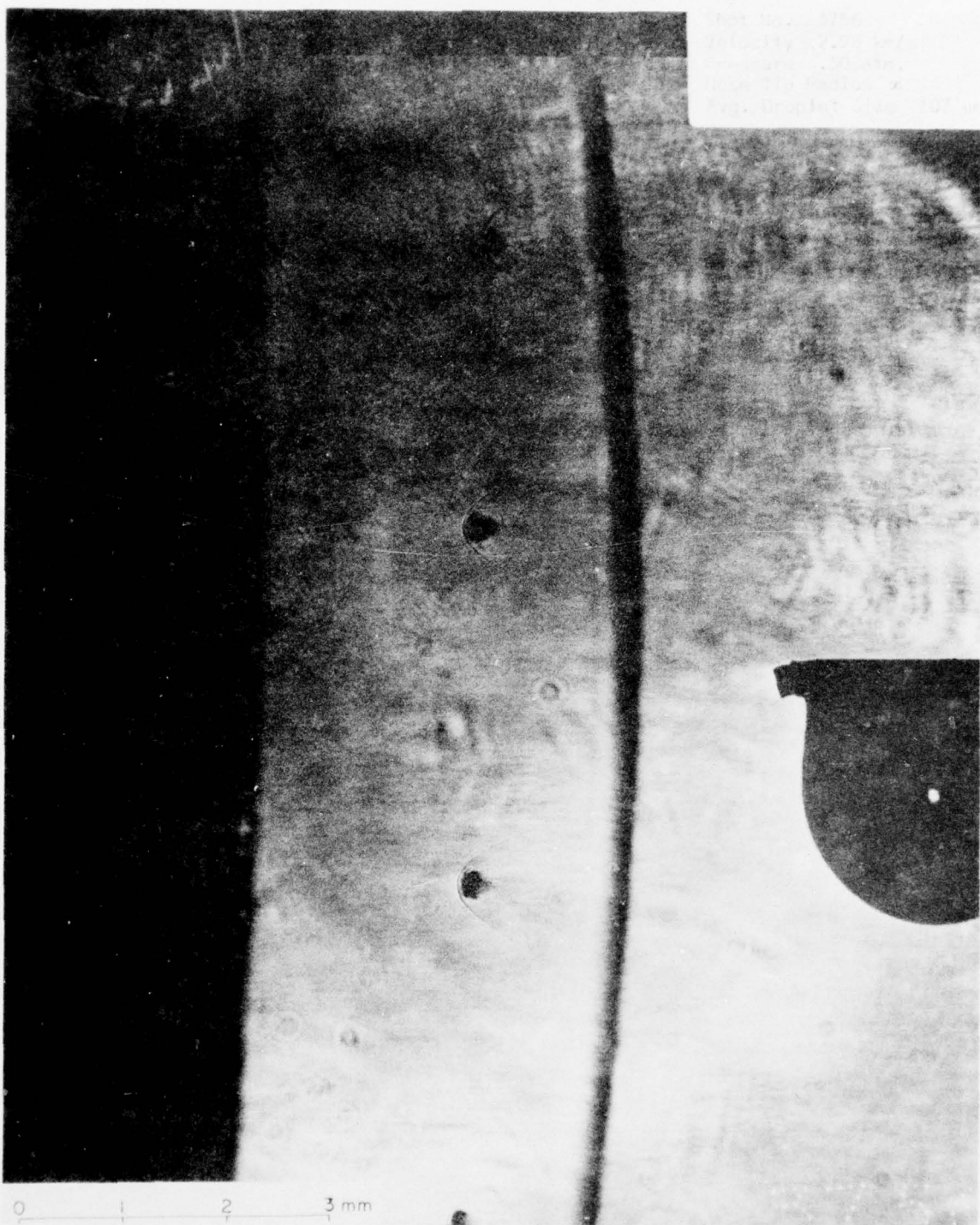
APPENDIX A
WATER DROPLET BREAKUP LASER SHADOWGRAPHS

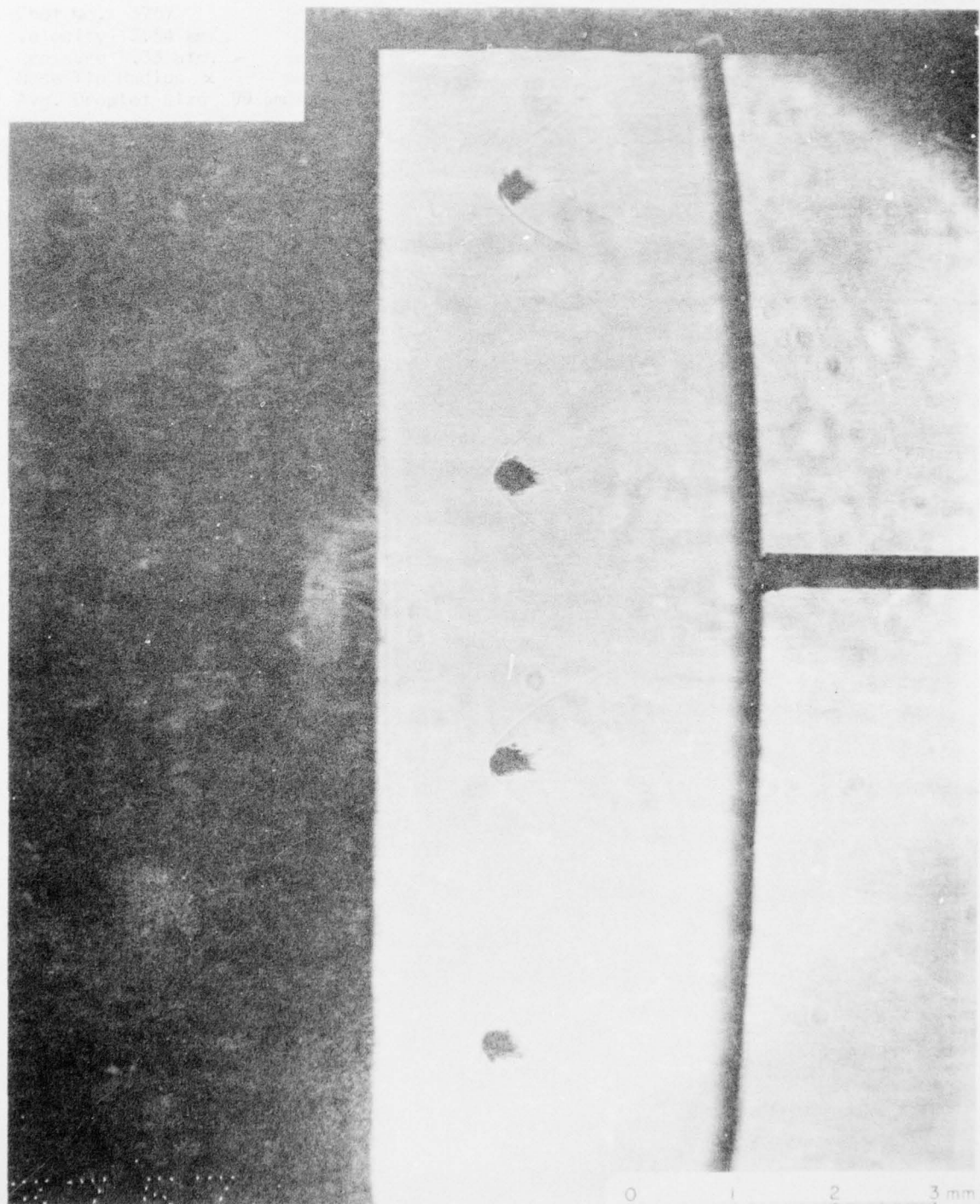
Shot No. 3783
Velocity 2.51 km/s
Pressure 1.13 atm.
Nose Tip Radius ∞
Avg. Droplet Size 108 μ m



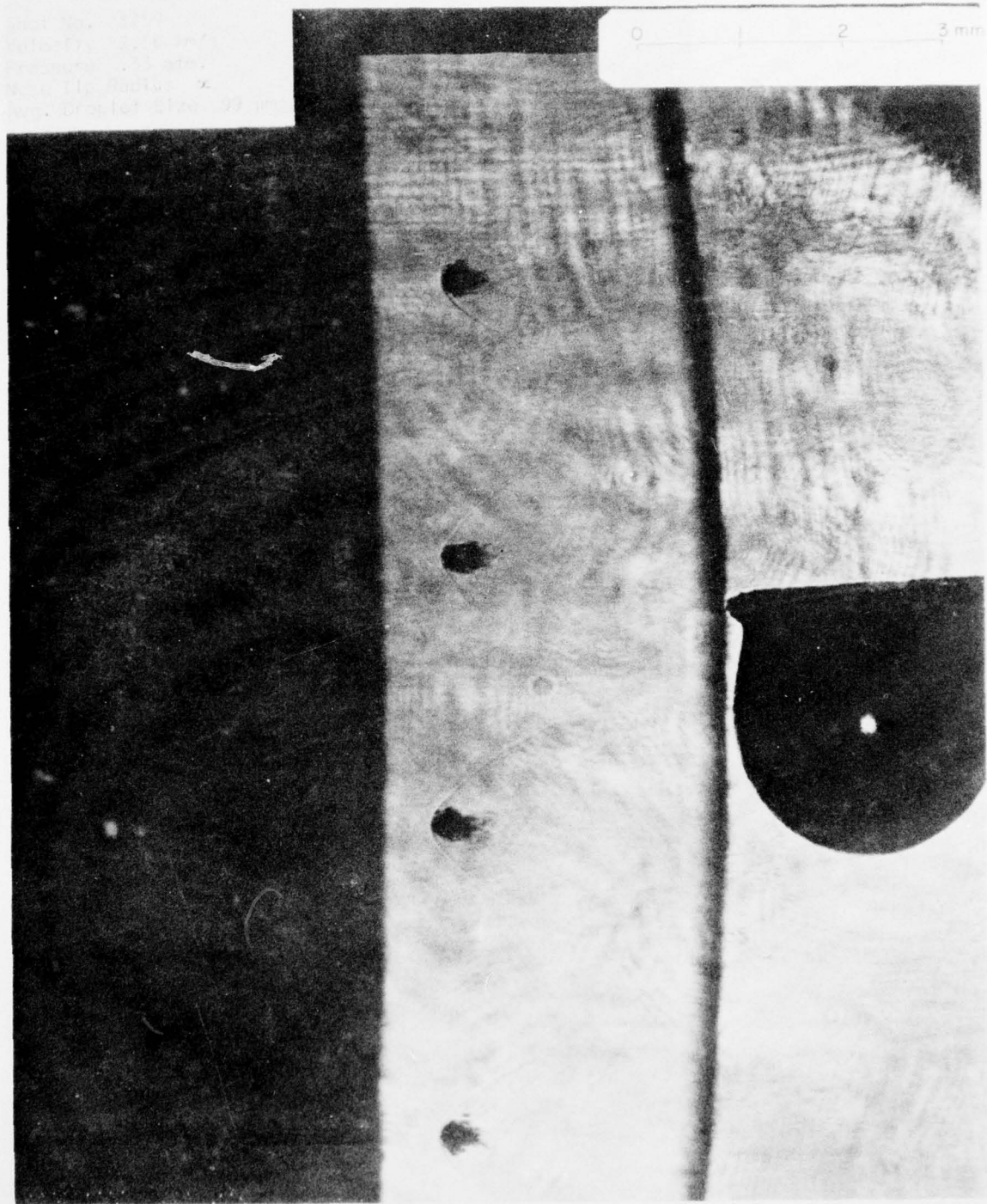
Hot Nov. 27, 1964
Velocity 1.4 km/sec
Pressure 1.7 atm
Nose Tip Radius 0.005
Reynolds Number 50,000



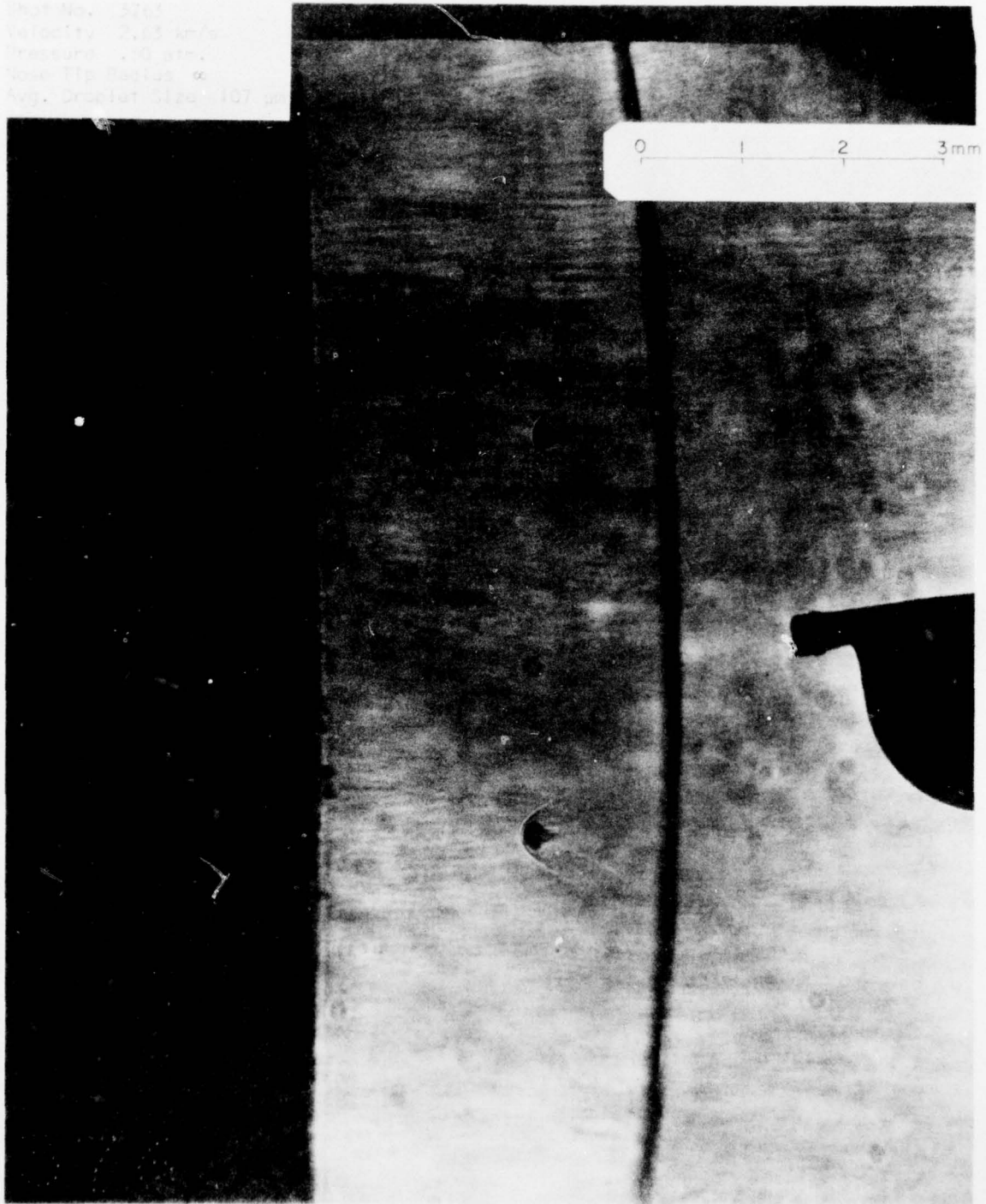




Spec No. 1000
Vaccinia, 100% confluent
monolayer, 24 hr.
Nov. 11, 1962. \times
approx. 1000 diam. 77 mic.

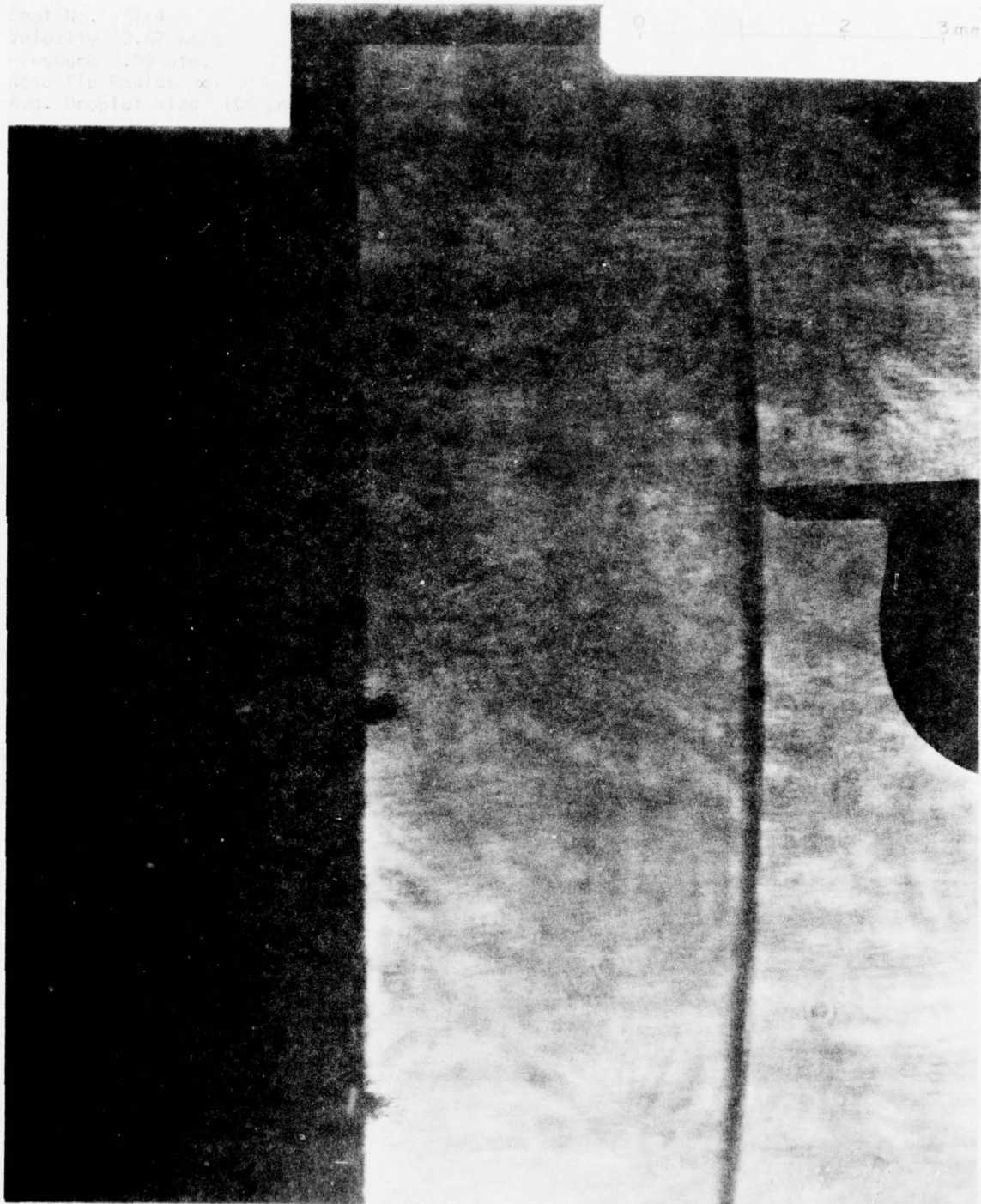


Shot No. 5265
Velocity 2.63 km/s
Diameter 1.0 mm
Time 11:56:12.00
Avg. Crater Size 107 μ



Inst. No. 1704
Velocity 2.07 mm/s
Pressure 170 atm
Noz. Tip Radius 0.005 mm
Avg. droplet size 1.63 mm

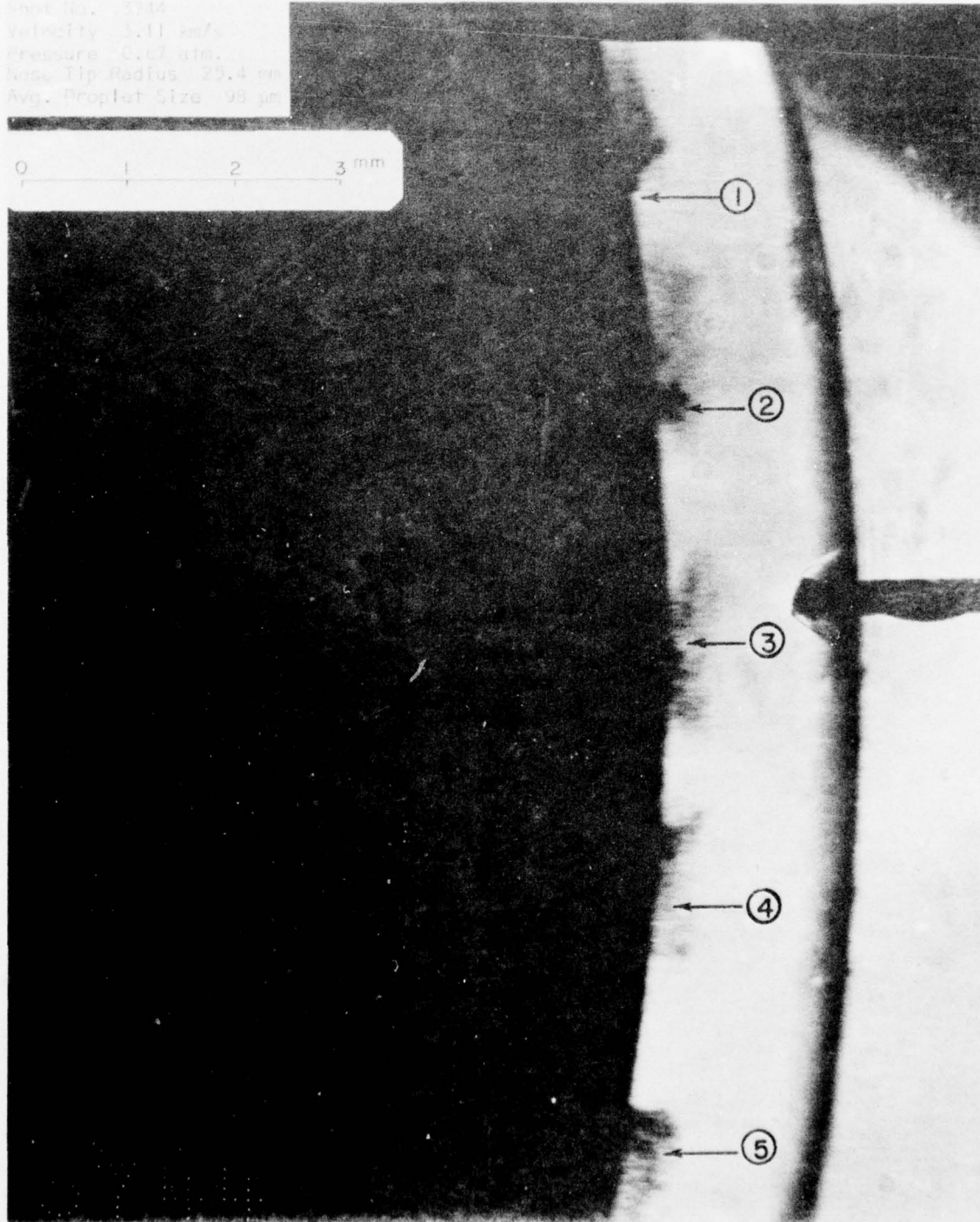
0 1 2 3 mm



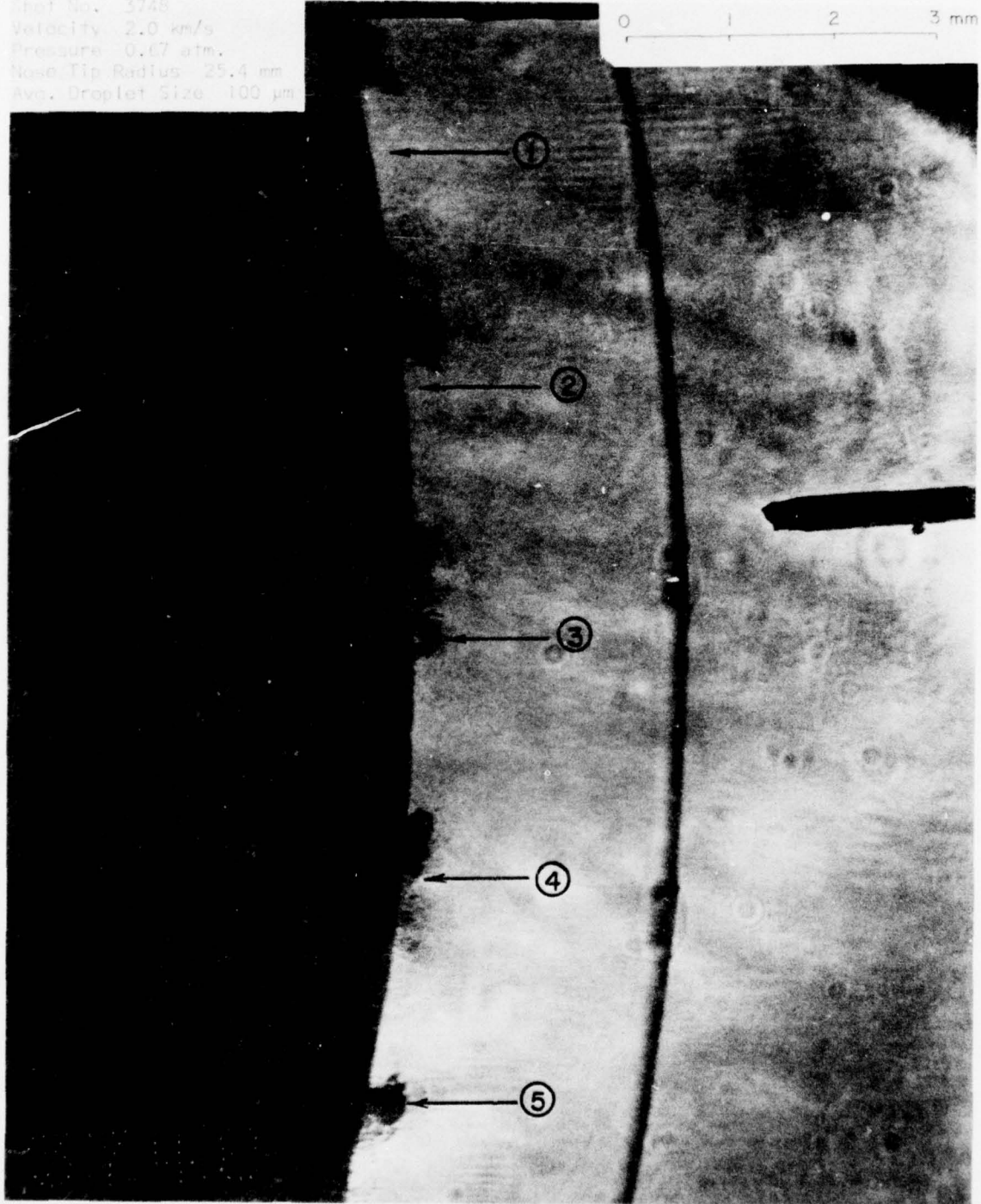
APPENDIX B
WATER DROPLET IMPACT LASER SHADOWGRAPHS

Flight No. 3714
Velocity 3.11 km/s
Pressure 0.07 atm.
Nose Tip Radius 29.4 mic
Avg. Droplet Size 98 μ m

0 1 2 3 mm

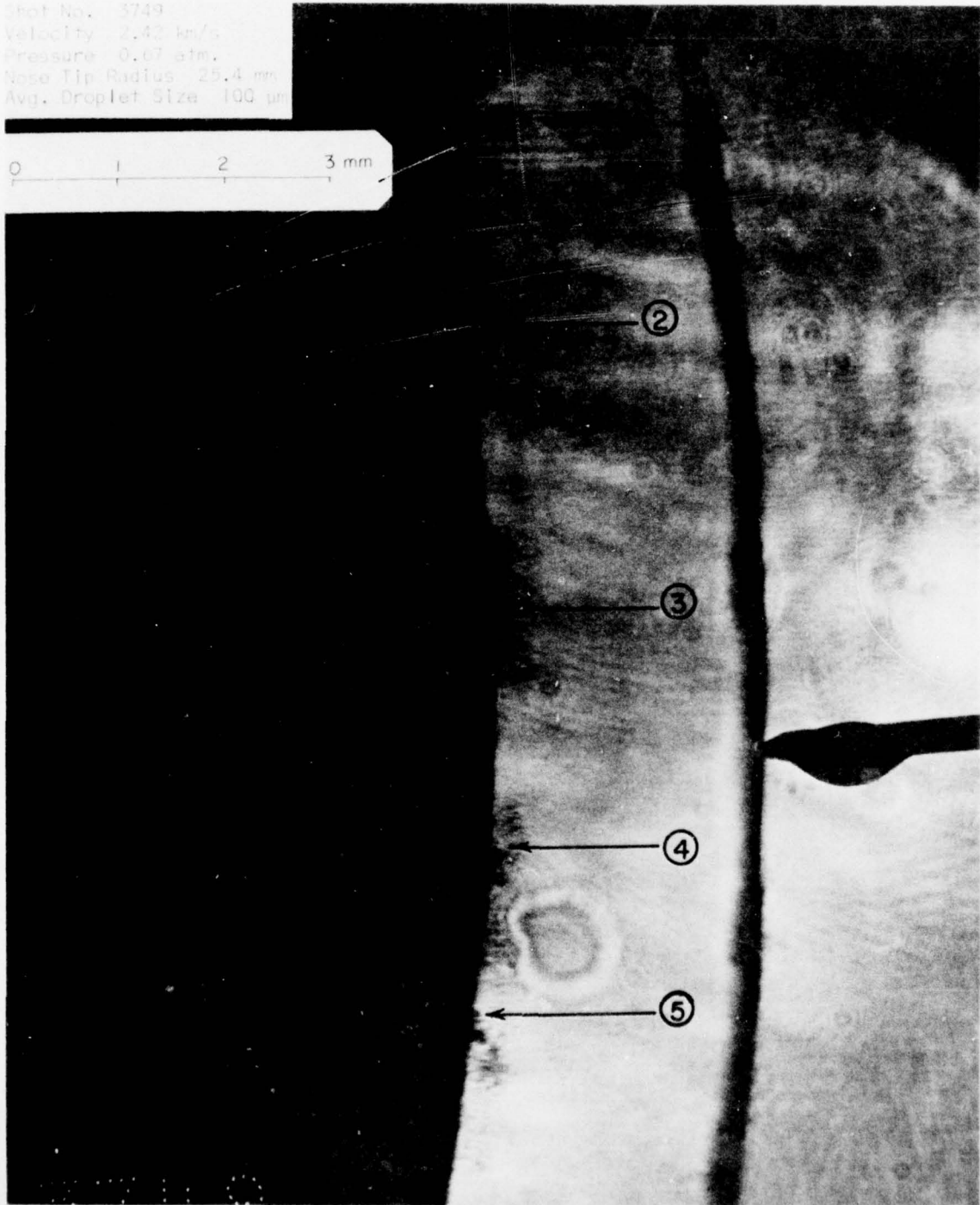


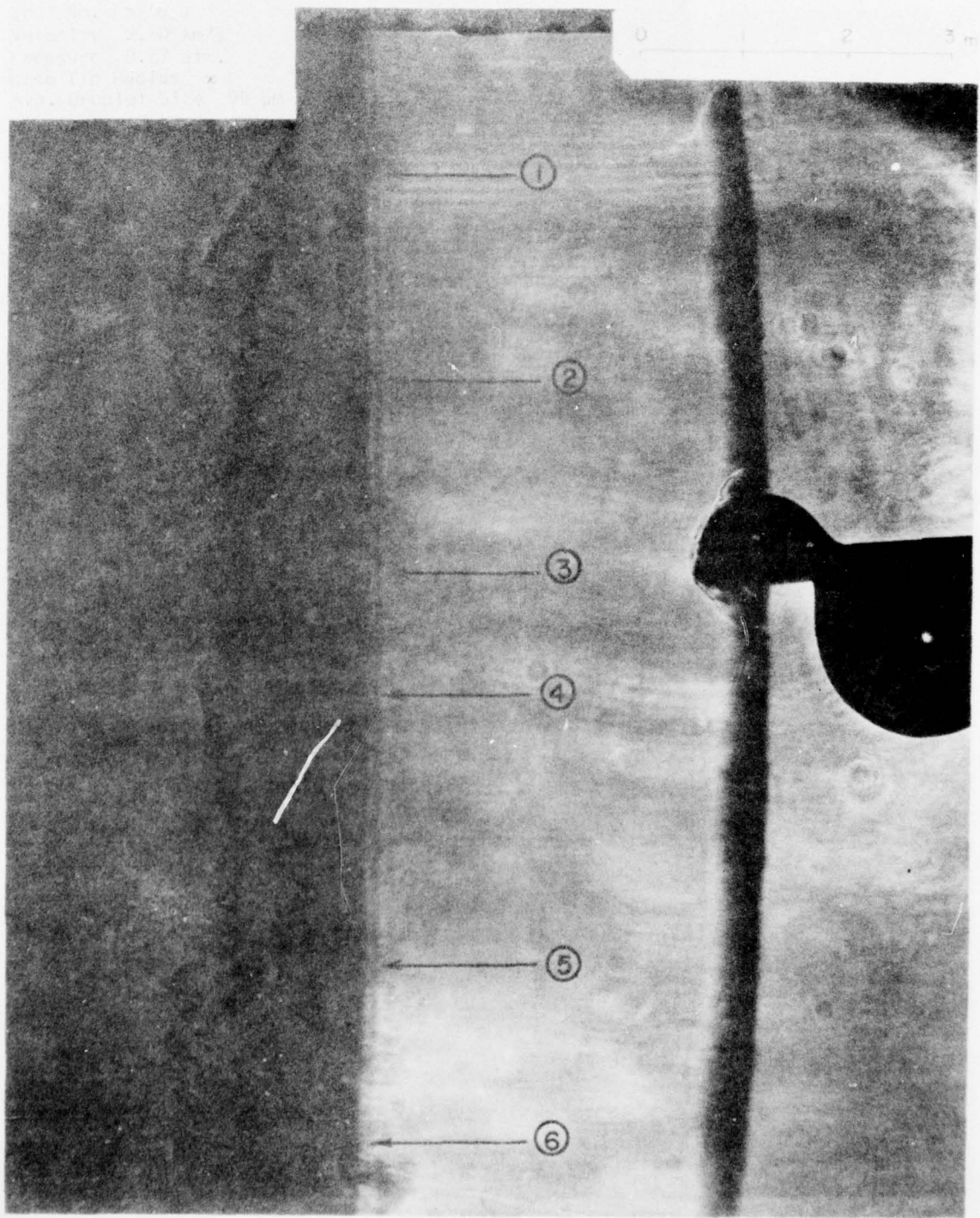
Shot No. 3748
Velocity 2.0 km/s
Pressure 0.07 atm.
Nose Tip Radius 25.4 mm
Avg. Droplet Size 100 μ m

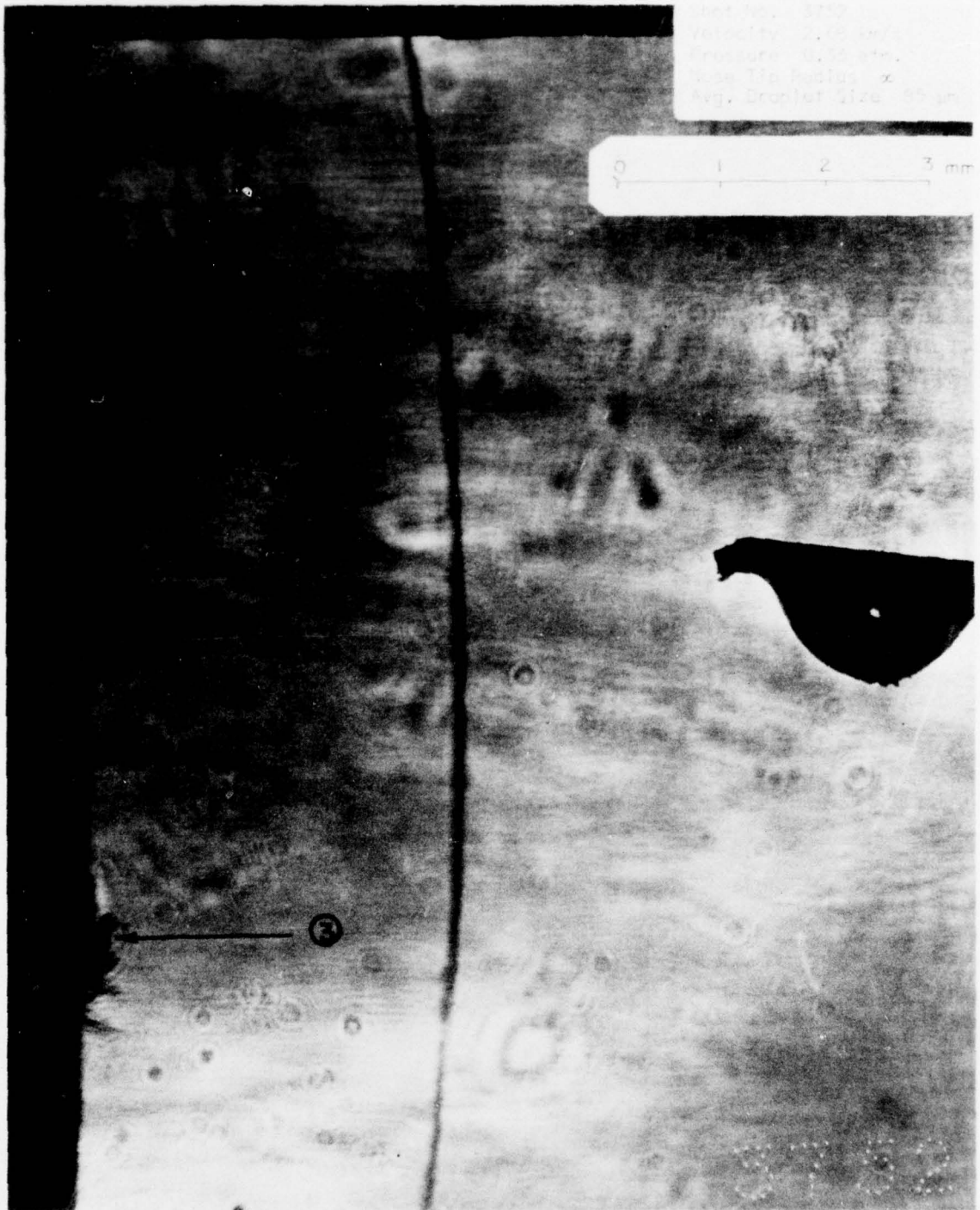


Shot No. 3749
Velocity 2.42 km/s
Pressure 0.07 atm.
Nose Tip Radius 25.4 mm
Avg. Droplet Size 100 μ m

0 1 2 3 mm







Shot No. 5760
Velocity 2.51 km/sec.
Pressure 0.50 atm.
Nose Tip Radius 1.8
Avg. Droplet Size 110 μ m

